INVESTIGATION OF SURFACE PHASE FORMATION DURING Sn-RICH GROWTH OF Cu_2ZnSnS_4 POLYCRYSTLALLINE THIN FILMS FOR SOLAR CELLS

by

Joseph Glenn Bolke

A thesis submitted to the faculty of
The University of Utah
in partial fulfillment of the requirements for the degree of

Master of Science

Department of Materials Science and Engineering

The University of Utah

December 2012

The University of Utah Graduate School

STATEMENT OF THESIS APPROVAL

The thesis of **Joseph Glenn Bolke**

has been approved by the following supervisory committee members:

Michael Scarpulla	, Chair	**6/11/2012** Date Approved
Ashutosh Tiwari	, Member	**6/11/2012** Date Approved
Richard Cohen	, Member	**6/11/2012** Date Approved

and by **Feng Liu** , Chair of the Department of **Materials Science and Engineering**

and by Charles A. Wight, Dean of The Graduate School.

ABSTRACT

Cu_2ZnSnS_4 (CZTS) is a semiconductor material made of nontoxic, earth abundant elements, making it a promising topic of research for absorber layers in thin film solar cells. We observed that rapid thermal annealing of tin (Sn)-rich co-sputtered CZTS films resulted in crystalline, hexagonal platelets of tin-disulfide (SnS_2) 5-30 μm long at the surface of the film. In this work, the formation mechanisms of these surface crystallites and their implications for CZTS absorber layer processing were investigated.

The formation and decomposition of these platelets were studied by observing the changes in their structural, morphological, compositional, and vibrational properties accompanying the imposition of lateral temperature gradients as well as different annealing atmospheres. The homogeneous co-sputtered films were annealed in a graphite boat in a quartz reactor using a base heater and halogen lamp. Interrupting annealings to examine stages of crystal formation showed at around 400 ^{o}C SnS_2 began to form on the surface of films.

Near the edges of the film, where temperatures were found to be higher, crystals melted into an amorphous unknown tin-sulfide phase. Diffusion of species from the film into the base of the crystals formed long CZTS grains of which the amorphous phase left behind as it coalesced. Annealing without sulfur (S) increased Sn and S losses from the film and increased the number of crystals nucleated on the surface of the film.

For solar cell device applications of CZTS thin films, removal of these SnS_2

surface crystallites is necessary; thus wet chemical and thermal decomposition etching techniques were studied. Wet etching attempts with KCN and NH_4OH solutions did little to etch crystals. HCl solution damaged the CZTS film as much as the crystals and therefore was also unsuitable. Thermal etching by evacuating the chamber near the end of annealing transformed the SnS_2 crystals into a grainy, S-poor Sn phase via the decomposition of SnS_2 by removing the vapor species with which it is in equilibrium. Understanding the role of Sn species during annealing is important for the complex CZTS system because small deviations from Sn stoichiometry results in drastic changes in the secondary phases and microstructure of the film. The experiments and insight provided in this thesis represent unexplored unconventional methods toward CZTS growth and different approaches for CZTS processing for development of thin film solar cell technology.

TABLE OF CONTENTS

LIST OF FIGURES

ACKNOWLEDGEMENTS

I would like to thank my wife, Stacey, for supporting me while I have been going to school, and my daughter, Kennedy, for her cheerful attitude in these challenging days.

I would also like to thank Doctor Mike Scarpulla for taking me on as an undergraduate researcher and shaping my educational career through this unique opportunity to be on the cutting edge of research and exploring the unknown.

I also thank my mentor Makarand Karmakar, and all the rest of the research group for all of the group meetings and lunch discussions brainstorming what is going on in CZTS.

CHAPTER 1

INTRODUCTION AND MOTIVATION

Throughout the world, the usage of oil and fossil fuels to supply energy is increasing, which is deepening mankind's dependence on these limited resources. In our own country, our consumption of natural resources for electricity and fuel causes us to rely on the imports from other countries to sustain our growth. For these reasons, electrical power plants are continually being built that produce electricity from natural gas, coal, wind, hydroelectric, and solar power. Solar energy is of particular interest because it is the only renewable resource with the capacity to be scaled up to supply the terawatts of electricity consumed by the world. Solar panels can be placed in many diverse locations worldwide, providing an infrastructure that is many times greater than the number of suitable hydroelectric and wind power locations. Using 10% efficiency panels, the 3.2 TW of power the US consumes could be supplied 1.7% of the area of the US [1]. No other renewable resource comes close to supplying power on this scale, but this type of realization requires mass production of photovoltaic modules on scales 100-1000 times larger than the 40 GW of total installed photovoltaic modules in the world in 2010.

In order to make solar energy a major source of electricity, photovoltaic technology needs to be cost competitive with current sources of electricity. There are several different approaches photovoltaic technologies take in order to be cost

competitive with other power sources. Silicon (Si) solar cells are the most common material used for solar cells and constitute 92% of the cells produced[2]. The well-developed semiconductor industry has resulted in cost-effective ways to achieve higher efficiency solar cells while a large portion of the costs are resting in the cost of the high purity Si substrate. Less efficient but less expensive Si solar cells have also been fabricated by using a lower quality solar grade multicrystalline Si [3].

Multijunction solar cells utilize organometallic vapor phase epitaxy to grow multiple solar cells on top of each other connected electrically in series. Each cell is optimized to extract the maximum voltage for different wavelengths of light in the solar spectrum. These are the most efficient solar cells reaching a record of 43.5% conversion efficiency under concentrated light [4]. Costs associated with producing multijunction solar cells are considerably higher than manufacturing of other cells because of the required epitaxy processes and expensive materials used. Because of the high costs, satellite and space applications are the only suitable uses without the use of concentrating optics. By concentrating light several hundred times using inexpensive mirrors or lenses, the light incident upon a large area is focused onto small cells in order to be cost competitive against other types of solar cell technologies.

Thin film inorganic solar cells based on cadmium telluride (CdTe) and copper indium gallium diselenide (CIGS) reduce production costs by using thin film techniques to deposit only thin layers of the semiconductor materials onto inexpensive substrates such as glass. These semiconductors have high absorption coefficients and make up the absorber layer in a cell. CIGS and CdTe are p-type without intentional doping due to the presence of defects. Because of difficulties associated with doping these materials n-type,

cells rely on a p-n heterojunctions to separate and collect the electron and hole (e^-/h^+) pairs. Materials with high absorption coefficients (>10^4 cm^{-1}) are especially suitable for these 1-10 μm-thick absorber layers by ensuring that a large portion of the incident light is absorbed. These polycrystalline solar cells are usually less efficient than single crystal silicon cells but are cost competitive with Si and other technologies by avoiding expensive single crystal processing steps, reducing materials usage, and the benefit of large area thin film processing techniques.

Less abundant elements (In, Ga, Se, Te) in the thin film solar cells mentioned are produced primarily as by-products of other metals mining operations such as copper and zinc. This is a potential limit on the manufacturing and commercialization of these solar cells due to production constraints [5]. Similarly, devices using the toxic element Cd are among the hazardous materials restricted by the European Union and China and raises concerns involving mass production of CdTe solar panels [6]. A relatively new alternative, copper zinc tin sulfide (Cu_2ZnSnS_4 or CZTS), utilizes only nonhazardous, earth abundant elements in order to overcome those limitations. It was derived from CIGS by substituting the rare group III elements in the crystal structure with Zn and Sn. Properties such as direct band gaps and processing techniques are common between CZTS and CIGS. The leading laboratory devices of CZT(S,Se) has performed at 10.1% conversion efficiency [7]. Although this is somewhat less efficient than the other technologies, it could prove a cost effective solution by utilizing less expensive materials and large scale processing.

CHAPTER 2

BACKGROUND

CZTS was originally developed for thin film solar cells in 1988 to utilize “more naturally abundant elements” than CIGS [8]. Since then, many deposition methods and electrical measurements have been performed in order to understand the physical processes and electrical behavior that govern its performance as a solar cell. Herein is discussed the electronic device behavior and processing methods for understanding CZTS use in thin film solar cells.

2.1 Operation of Thin Film Solar Cells

Thin film solar cells rely on a p-n heterojunction and semiconductor materials with a high absorption coefficients to convert energy from light into electricity. A cross sectional view of complete thin film solar cells is laid out in Fig 2.1. At the heart of a photovoltaic cell is a planar p-n junction created by the p-type absorber and the n-type transparent conductive oxide (TCO). The TCO is degenerately doped in order to extend the space-charge region of the p-n junction deep into the absorber layer. As electrons absorb photons of light with energy greater than the energy band gap (Eg) of the absorber semiconductor, they are promoted to higher energy states located in the conduction band and leave an empty state (hole) in the valence band. The electric field in the space charge

region serves to move excited electrons in the conduction band away from holes in the valence band maintaining a voltage for recombination through an external circuit.

Semiconductor absorption behavior depends strongly on its Eg. Semiconductors will show poor absorption of light with photon energies below the Eg because there are no transitions between states to allow electrons to absorb the photons. This fact makes large Eg semiconductors useful to make a p-n junction with the absorber layer because they allow most of the intensity of light to reach the absorber layer and are referred to as window layers. Materials with a direct Eg, such as CdTe, CIGS, and CZTS exhibit an Eg minimum at transitions between valence and conduction bands at a zero momentum vector, which allows photons to be easily and efficiently absorbed if they have energies above the Eg. Materials with an indirect Eg such as Si and Ge exhibit an Eg minimum between points of different momentum vectors. This requires assistance from lattice vibrations in the crystal to absorb photons with energies above that Eg and therefore exhibits lower absorption of photons until photons with high enough energies can make more direct transitions. Fig 2.2 shows this by comparing the absorption coefficient α, of these two Eg types versus photon energies. Small values of α require thicker layers in order to absorb the incident light. In the case for thin film solar cells, direct Eg materials have high values of α allowing them to efficiently absorb a majority of light as long as it is above the Eg of the material.

In addition to selecting a material with a high absorption coefficient, the power output of a solar cell is the product of the electrical current and voltage produced, both of which are dependent on the Eg of the material. The voltage output from a solar cell increases with increasing Eg because of increased potential between valence and

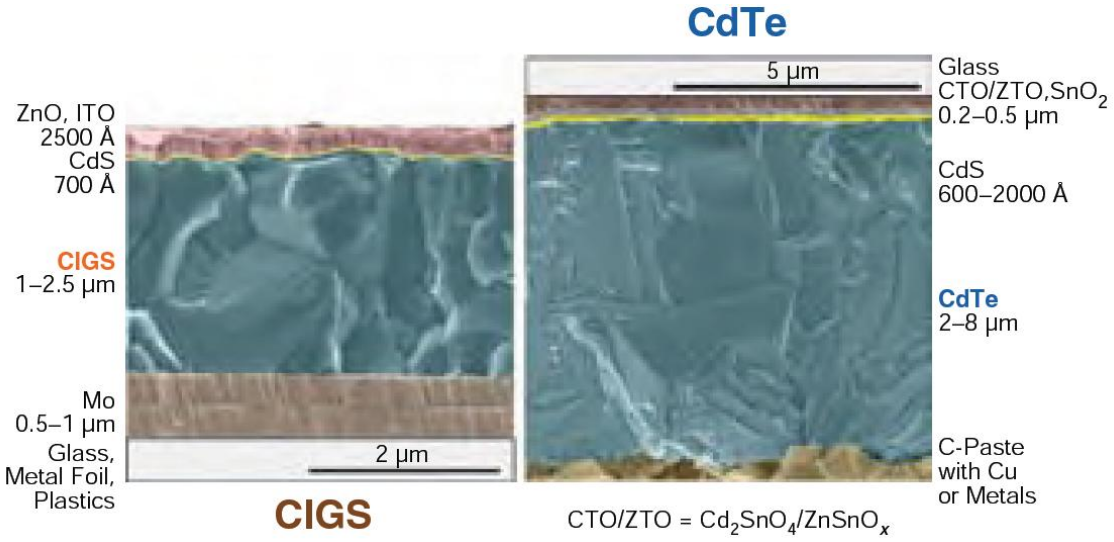

Figure 2.1: Cross-sectional SEM view of a CIGS and CdTe thin film solar cells with each layer colored and labeled. Light absorption in the thicker absorber layers produces e-/h+ pairs which are separated by the heterojunction and conducted to the transparent conductive oxide and metal contacts. From [9], used with permission.

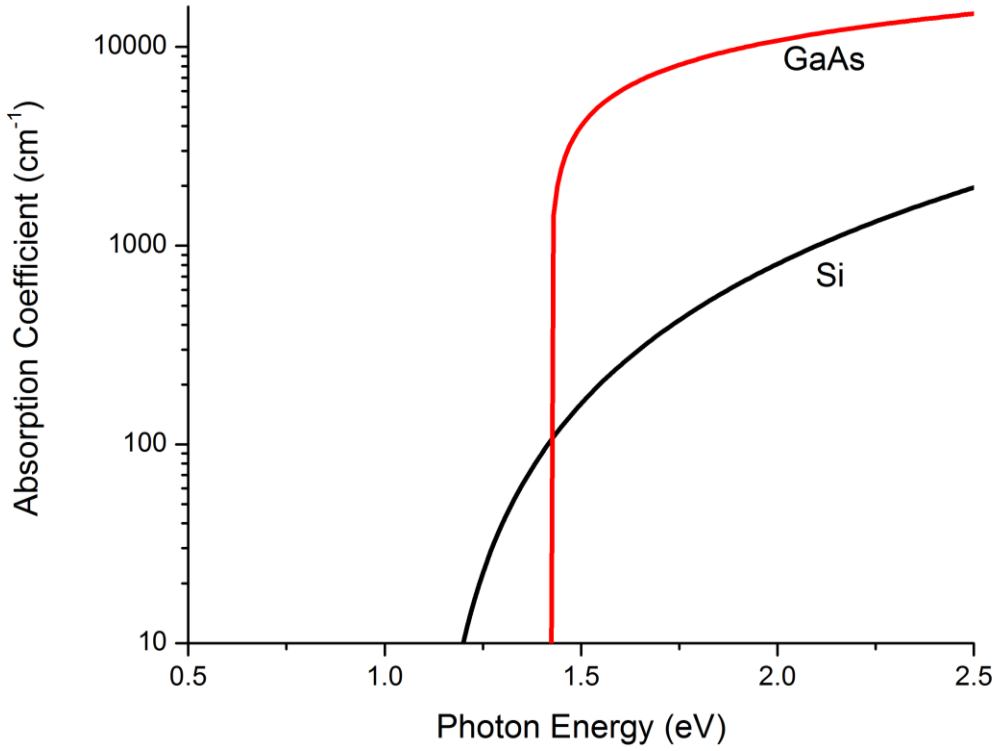

Figure 2.2: Absorption coefficient α for GaAs and Si versus photon energy. Materials such as GaAs with a direct Eg show high absorption of photons with energies above their Eg, whereas Si shows a more gradual increase in α with increasing photon energy due to its indirect Eg.

conduction bands. However, the current output is dependent on the number of photons absorbed. Materials do not absorb photons with energy less than Eg, therefore decreasing Eg captures more of the solar spectrum and increases the current produced. The optimization of these two competing processes was originally calculated by William Schockley and Hans Queisser in 1961. Fig 2.3 shows this calculation and an adjustment made to compensate for the output voltage of a solar cells being less than the Eg. This makes CIGS and CZTS good candidates for solar materials based on optical absorption because they have been shown to have a tunable direct Eg's in the optimum 1.5 eV range with elemental variation (In/Ga in CIGS [10] and S/Se in CZTS [11, 12]).

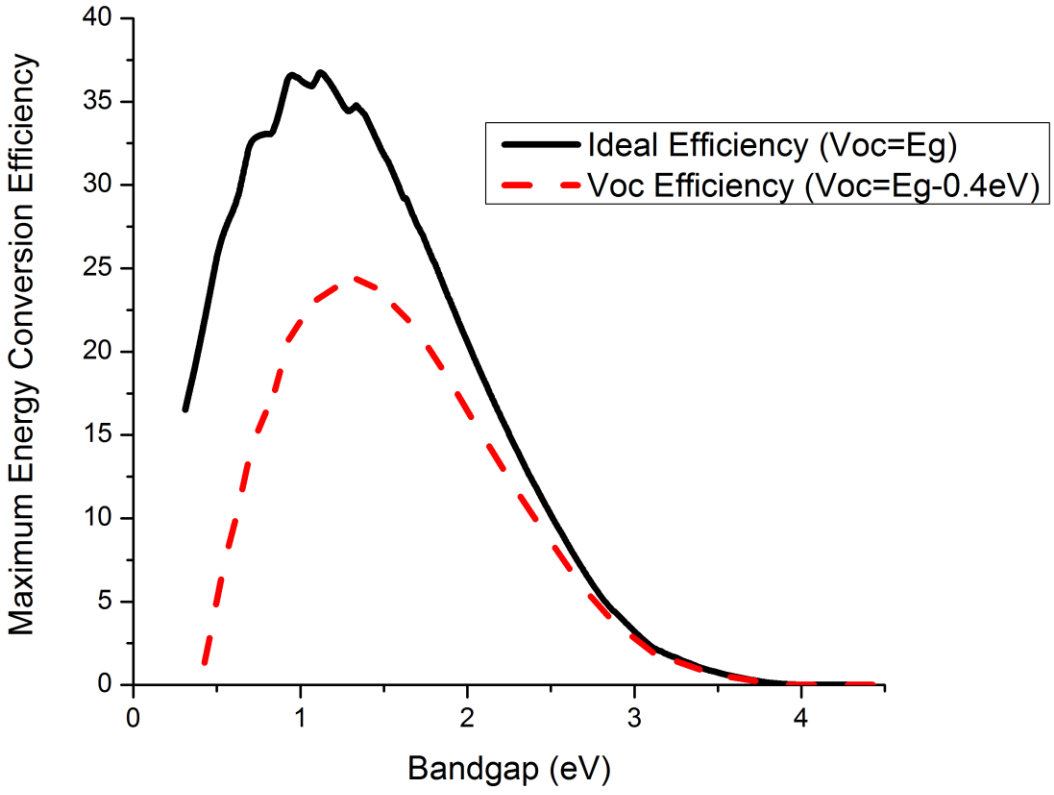

Figure 2.3: Calculation of the Schockley-Queisser efficiency limit showing the maximum power conversion efficiency dependence on the Eg of the semiconductor for a single p-n junction using ideal and realistic efficiencies.

Light that is absorbed outside the depletion zone depends on the minority carrier diffusion to reach the space charge region before it recombines in order to be separated for use in the circuit. Recombination wastes the energy absorbed from the light by converting it into heat and is a major cause of reduced efficiencies. The mean diffusion length of minority carriers is determined by the minority carrier lifetime and mobility in the absorber layer. Most solar cells are designed to absorb photons primarily in the p-type layer of the junction because electron mobilities are typically several times larger than the hole mobilities. It is crucial that the distance between where the carriers are generated and the depletion width is less than the diffusion length or else most carriers are going to recombine before separating. Because CZTS is a polycrystalline material it has higher concentrations of defects at grain boundaries which trap carriers and assist recombination [13]. Large grain sizes are sought after in the absorber in order to reduce recombination from intergranular conduction [14].

2.2 Deposition of CZTS Absorber Layer

CZTS is commonly deposited on molybdenum(Mo) coated glass with Mo serving as the electrical back contact to the cell. As a refractory metal, Mo does not melt or diffuse into the CZTS at the processing temperatures involved. Other processing parameters important to the development of CZTS involve the composition. It has been shown that the stoichiometry of the CZTS film affects the grain growth and efficiency [15]. Record CIGS cells performing around 19% energy conversion efficiencies were developed using co-evaporation to carefully control deposition rates of each source and shift stoichiometry of the growing film [16]. This takes advantage of specific growth

properties of Cu-rich compositions which flux the growth of large CIGS grains by creating a copper sulfide (Cu-S) secondary phase at grain boundaries. At the elevated processing temperatures, the Cu-S phase has a high mobility of the Cu^+ species. This enhances crystallization of the CIGS grains by providing higher mobility for indium and gallium via the Cu-S phase. If not removed, this electrically conductive copper phase will remain at grain boundaries and cause recombination of carriers and shorting of the cell. Methods of removing this secondary phase include wet chemical etching with KCN or following the growth of the Cu-rich films with a Cu-poor composition to fully react the Cu-S species. KCN etching can lead to porous films, which have problems with leakage currents in the cell due to pinholes. Leaving the film Cu-poor has been shown to be important to both CIGS and CZTS films because Cu vacancies serve as shallow acceptors and is essential to absorbers with suitable electronic properties [17].

Co-sputtering from metal or binary sulfide targets is a versatile way to control stoichiometry during deposition of CZTS. Co-sputtering results in a film which reacts quickly at elevated temperatures due to proximity of species because species are evenly distributed [18]. The microstructure of the film can be controlled to form columnar grain growth and reduce grain boundaries in e^-/h^+ paths. Thermal evaporation techniques are used to avoid the ion-damage that results from sputtering techniques. However, instabilities of Sn oxidation state has resulted in problems growing CZTS like CIGS in thermal evaporation [19]. Both these methods require high vacuum conditions but are useful for large area deposition. Other thin film techniques such as electrodeposition [20] and solution-based techniques [21] avoid operating in vacuum to remove costs of vacuum equipment and problems associated therein.

Processing of the CZTS absorber layer can be done in a single step using heated substrates to react the film during deposition; however an annealing step following deposition is effective for growing grains and fully reacting the precursors. The formation reaction of CZTS involves the following sulfide species according to the path:

$$Cu_2S_{(s)} + SnS_{2(s)} \rightarrow Cu_2SnS_{3(s)} \qquad \text{Reaction 1}$$

$$Cu_2SnS_{3(s)} + ZnS_{(s)} \rightarrow Cu_2ZnSnS_{4(s)} \qquad \text{Reaction 2}$$

These steps, done in a high temperature sulfur atmosphere, ensures sufficient sulfur is supplied to the film to form the binary sulfides so that S is not the limiting reagent for maximum CZTS formation. Use of this annealing step is one of the developments to reduce the instability of the Sn species in order to form suitable CZTS films for photovoltaic cells [19].

The important role that the S pressure plays is demonstrated in Table 2.1 which gives the oxidation reaction for some of the possible reactions that can be in equilibrium with S_2 vapor such that the dependence of oxidation state relies on the temperature and S_2 pressure. Each of these equations takes the form xA + S_2 ↔ yB where A and B are the solid phase reactant and product respectively. This allows the calculation of the equilibrium pressure of S_2 required to stabilize the oxidation state of metal using data in Table 2.1 and the following thermodynamic relationship:

$$\Delta G = \Delta H - T\Delta S = -RT \ln\left(\frac{a_A{}^x}{a_B{}^y \dfrac{P^{s_2}}{P_o^{s_2}}}\right) \qquad (2.1)$$

where ΔG, ΔH, and ΔS are the changes in Gibbs free energy, enthalpy, and entropy respectively; T is the absolute temperature, R is the gas constant, and P^{S2} and P_o^{S2} are the pressure of S_2 in the system and the standard pressure. Assuming components A and B to be pure substances and their activity a_A and a_B to be 1, then the equation can be simplified and solved for the partial pressure of S_2.

$$\log\left(\frac{P^{S_2}}{P_o^{S_2}}\right) = \left(\frac{\Delta H - T\Delta S}{2.3RT}\right) \tag{2.2}$$

Fig 2.4 shows the equilibrium P^{S2} calculated for each transition in oxidation states for the metals. In order for a higher oxidation state to be stable for the element, the pressure of S_2 must be above the line shown for that transition. The instability of the Sn in the 4^+ oxidation state results from the high S_2 pressure required to stabilize the sulfide, which ZnS and Cu_2S do not have.

2.3 Forming the p-n Junction

To complete a CZTS solar cell a p-n junction is formed with n-type Al doped ZnO with a buffer layer of n-type CdS between the two. The CdS buffer layer is typically 50 nm thick and is deposited by chemical bath deposition. CdS deposited this way shows uniform coverage of the absorber effectively reducing shunting paths in the solar cell [22]. Because CdS is difficult to heavily dope, a highly doped ZnO layer is required in order to extend the depletion zone into the absorber to increase collection efficiency of carriers and reduce recombination in the CdS. The CdS provides another service by reducing the sharp band offsets between the ZnO and CZTS. Cells are finished with Ni/Al electrical contacts and an antireflective coating.

Table 2.1: Thermodynamic Data for Sulfide Reactions

Reaction	*Free Energy Change (cal)*	*Temperature Range (^oC)*	*Source*
$2Zn+S_2 \leftrightarrow 2ZnS$	-128471+45.73T	25-420	[23]
$2Zn+S_2 \leftrightarrow 2ZnS$	-131095+49.48T	420-1200	[23]
$4Cu+S_2 \leftrightarrow 2Cu_2S$	-63945+17.22T	103-435	[32]
$4Cu+S_2 \leftrightarrow 2Cu_2S$	-62109+14.63T	435-1067	[32]
$2Sn+S_2 \leftrightarrow 2SnS$	-84571+46.22T	232-599	[32]
$2Sn+S_2 \leftrightarrow 2SnS$	-82318+43.60T	599-860	[32]
$Mo+S_2 \leftrightarrow MoS_2$	-84700+53.27T	25-719	[32]
$4SnS+S_2 \leftrightarrow 2Sn_2S_3$	-56000+47.78T	25-599	[32]
$2Sn_2S_3+S_2 \leftrightarrow 2SnS_2$	-53200+49.07T	25-760	[32]
$2Cu_2S+S_2 \leftrightarrow 4CuS$	-44295+49.86T	25-507	[32]

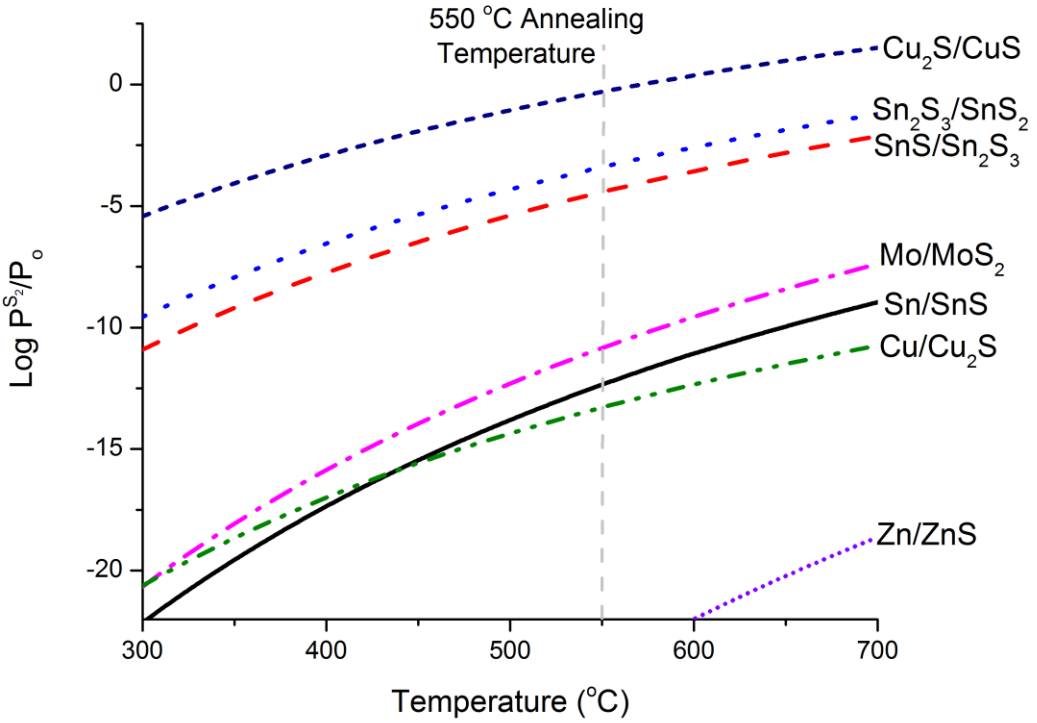

Figure 2.4: Equilibrium pressure of S_2 for each oxidation state of material. Lower oxidation states are favorable at the lower pressure. Of the CZTS precursors, only SnS_2 is unstable in contact with Mo metal at the annealing temperature of 550 ^oC.

2.4 CZTS Secondary Phase Effects

During the annealing of a CZTS absorber layer, secondary phases often arise from incomplete or parasitic reactions. The secondary phases observed usually are strongly influence by the stoichiometry of the film and affect the morphology of the film. Due to narrow solubility limits of CZTS, any deviation from stoichiometry results in CZTS in equilibrium with one or two other phases as can be seen in Cu_2S-ZnS-SnS_2 pseudo-ternary system in Fig 2.5. Annealing in low S pressure atmospheres results in insufficient formation of the reacting species limiting the CZTS formation and introduces even more phases not mentioned in Fig 2.5.

Annealing of metal precursors in S have been shown to play a role in developing the morphology as the film as it reacts to form CZTS. This is well illustrated in Fig 2.6 for layered precursor films with the Zn-rich and Cu-rich stoichiometries. In the case of Zn-rich, ZnS is left unreacted on the surface of the film and can interfere with the additional processing steps to form a solar cell and introduce more series resistance to the cell. The Cu-rich case illustrates how a Cu-S phase can assist grain growth but introduces excess Cu-S or Cu-Sn-S species that can form inclusions or pin-holes in the film after KCN etching of those phases. Phases of the lower Eg Cu_2S (Eg =1.21 [24]) embedded in CZTS causes trapping and recombination of electrons and holes that come in close proximity of the phase. This lowers the current produced by the cell, which is why alternative growth conditions need to be explored.

Sn in CZTS is in the 4^+ oxidation state and has been found to be a limiting factor for annealing temperatures and times due to preferred preference for the 2^+ state at elevated temperatures [19]. Without careful control of annealing parameters, volatile SnS

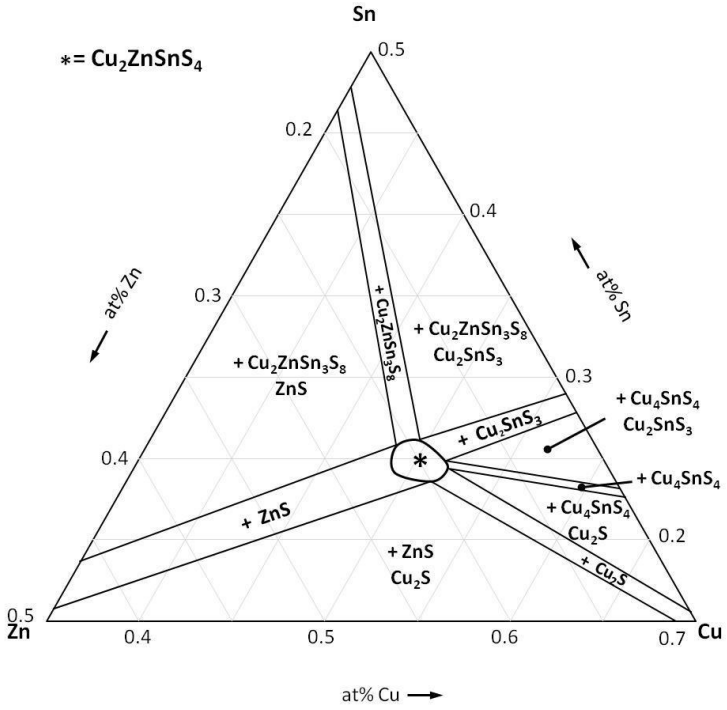

Figure 2.5: A section of the pseudo-ternary phase diagram of sulfide precursors at a 400 ^{o}C isotherm with expected phases in each region labeled. From [25], used with permission.

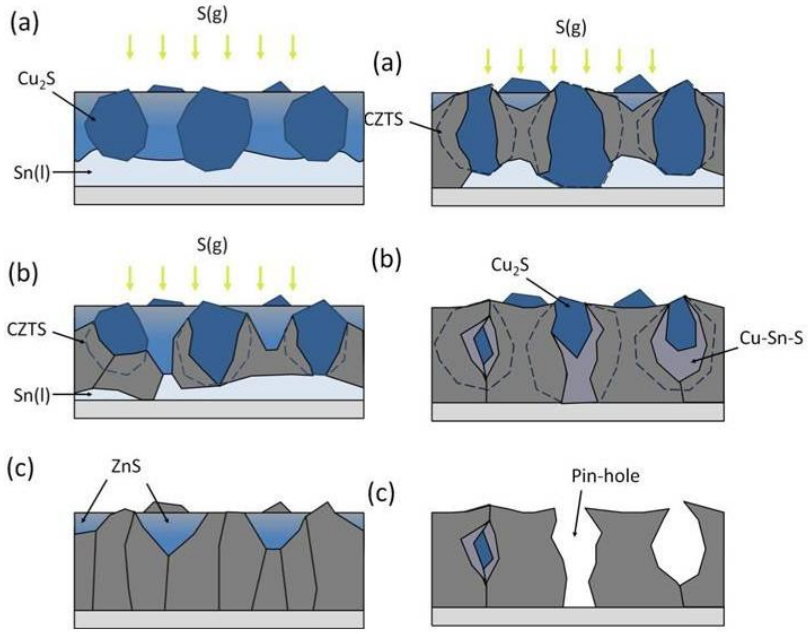

Figure 2.6: Stages of CZTS formation under Zn-rich (left) and Cu-rich (right) compositions and Cu_2S, ZnS, and Sn as precursors. The low melting point of Cu2S helps grains to fuse and grow larger than the Zn-rich case. These secondary phases define the morphology observed. (c) on the right shows the effect of KCN etching to remove Cu-S phases. From [25], used with permission.

can be produced from the decomposition of CZTS. This decomposition leaves behind secondary phases and thereby reduces the quality of the CZTS absorber. An approach to address these problems is Sn-rich growth. This research project initially aimed to test whether Sn-rich conditions could be used to grow larger grains of CZTS analogous to the Cu-rich growth of CIGSe and CZTS. Although this was not observed, Sn-rich growth and related secondary phases were investigated to understand the relationships of CZTS growth with the Sn species, as well as test the possibility of Sn secondary phases stabilizing CZTS by preferentially decomposing before allowing CZTS to decompose.

CHAPTER 3

EXPERIMENTAL PROCEDURES

Experiments on annealing were conducted on samples cut from the same co-sputtered CZTS absorber precursor layer. This precursor was deposited on 1" x 3" soda-lime glass coated with 500 nm of stress relieved molybdenum (Mo). Mo stress relieving reduces delamination of the CZTS film from the Mo and was done by sputtering in a Denton Discovery 18 by first achieving a base vacuum pressure of $2x10^{-6}$ Torr and then backfilling with argon to a pressure of $5.7x10^{-3}$ Torr and sputtering with a power of 300 W for 1 minute followed by 200 W for 2 minutes at $2.3x10^{-3}$ Torr. This caused a tensile stress at higher power and pressure and compressive stresses at the lower power and pressure and was repeated seven times and ended with 300 W at $5.7x10^{-3}$ Torr; resulting in a total film thickness of about 500 nm and a stress-balanced film.

Co-sputtering of the CZTS precursor films were deposited in a sputtering system equipped with three 75-mm diameter Lesker Torus® sputtering sources, LN_2 cooled tubing, and a turbomolecular pump backed by a rotary vane pump. The Mo-coated samples were loaded in the system and the chamber was evacuated to a base pressure of $2x10^{-7}$ Torr. The chamber was backfilled with argon to a pressure of $5.0x10^{-3}$ Torr and the substrated was plasma cleaned for 10 minutes at 100 W RF bias. The power was then switched to the three targets which consisted of Cu_2S (106 W), ZnS (44 W) and SnS_2 (87

W) (Plasmaterials, Livermore, Ca 99.5% or higher), and were sputtered 30 minutes. The pressure was then reduced to 2.0×10^{-3} Torr for 120 minutes. Initially depositing at higher pressure increases the deposition rate and improves adhesion to the Mo, then dropping the pressures lowers the deposition rate and reduces stress and cracking in the film. The final film thickness was found to be around 2 μm from cross-sectional SEM.

Annealing of this precursor film was done in a graphite boat in a quartz chamber. The boat was loaded with 200 mg S powder and 26 mg Sn metal in reservoirs cut into the ends before every annealing unless otherwise stated. The setup of the annealing system is illustrated in Fig 3.1 as well as where samples are place. A lid was placed on the boat to help maintain the reactive atmosphere in the boat. Thermocouples were placed near the sample and base heater to monitor the approximate temperature of the boat during annealing. The chamber was then evacuated and purged repeatedly with a forming gas (4% H_2, 96% N_2) and sealed at a pressure of 90 kPa. The base heater raised the temperature of the samples to 300 ^{o}C before turning on the halogen lamp. This lamp was ramped up to 85 V over 25 minutes and held for 30 minutes in which temperatures rose to 550 ^{o}C in the boat. The base heater temperature remained around 400 ^{o}C by reducing power in order to prevent decomposition of the heater above 400 ^{o}C. Similar ramping down was performed afterward and the samples were allowed to cool before venting the chamber. Temperature profiles for the boat and base heater are depicted in Fig 3.2. Sn in the recesses in the boat served to saturate the vapor in the boat with SnS. After annealing, none of the initial S remained and lumps of a Sn-S phase was found in the boat. Small deviations from this annealing recipe were tested in order to observe their effects on the formation of the film, surface phases, as well as edge effects. Thermal gradients were

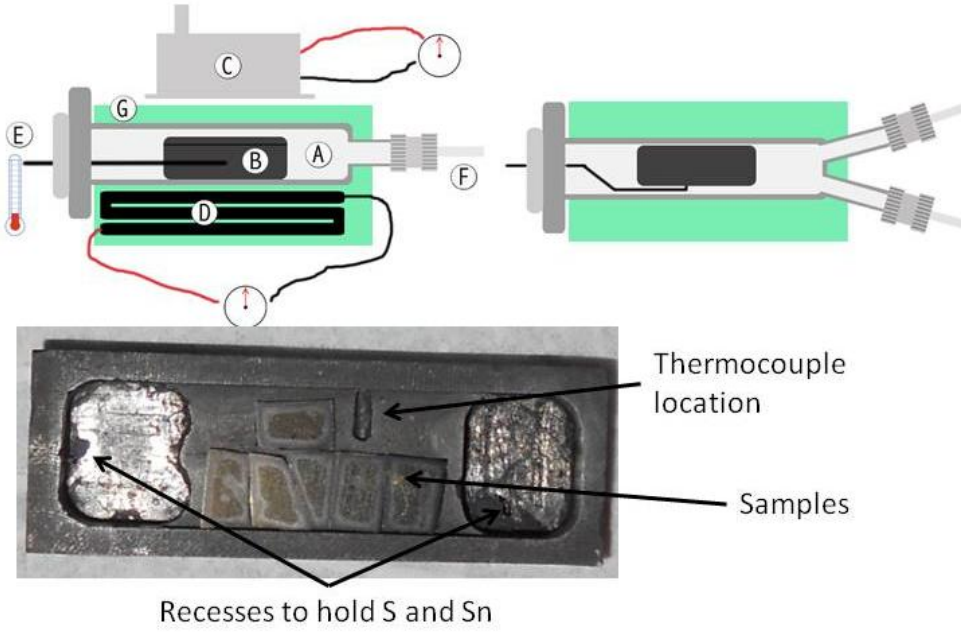

Figure 3.1: The equipment in the annealing arrangement side-view (left) and top-view (right). The quartz annealing chamber (A) with the graphite boat (B) was heated with a halogen lamp (C) and resistive base heater (D). A thermocouple (E) monitored the approximate temperatures inside the boat. The chamber was evacuated and purged each with a tube with valves (F). A firebrick (G) insulated the chamber and heater to maintain high temperatures. Recessed bays allowed Sn and S to be loaded into the boat while avoiding contact with the sample.

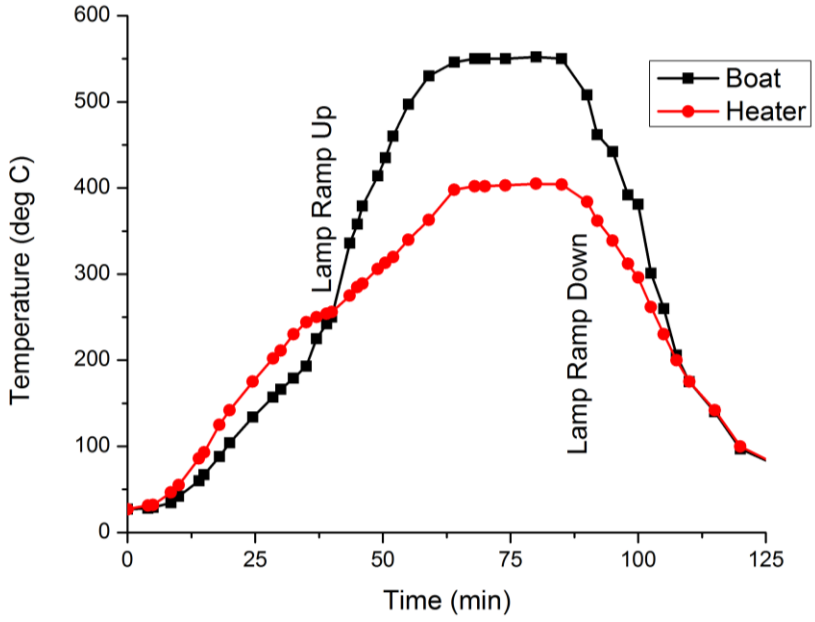

Figure 3.2: Annealing temperature profiles for the graphite boat and base heater for annealing procedure. Experiments interrupting ramp up during heating showed that most of the sulfur powder is gone when temperatures reach 400 ^{o}C.

tested by masking the quartz chamber with a strip of aluminum foil effectively shadowing a quarter of the boat. The shadow made a cooler side of the lid but did not directly cover the samples.

X-ray diffraction (XRD) was done using a Philips PANalytical MPD in Bragg-Brentano geometry and analyzed with X'Pert HighScore Plus software. High magnification electron micrographs of the absorber layers were taken with a Hitachi S-3000N scanning electron microscope (SEM) equipped with an EDAX Phoenix X-ray analyzer to perform energy dispersive spectroscopy (EDS). Electron beam interactions to produce X-rays were simulated using CASINO v2.4 Monte Carlo simulator to understand interaction volumes of the electrons in the sample [26]. Micro-Raman spectroscopy was performed using a Witec Alpha confocal microscope with a 532 nm laser and a 60x objective lens in order to identify surface phases in conjunction with compositional data from EDS.

Etching of samples in KCN was done using a solution of 5 weight percent KCN in deionized (DI) water for varying amounts of time and afterward rinsed with DI water. NH_4OH and HCl solutions were also used to explore effects on the film and secondary phases.

CHAPTER 4

RESULTS AND DISCUSSION

4.1 Characterization of Film and Surface Phases

All films annealed in this study were of the same Sn-rich Cu-poor composition and every film formed thin hexagonal SnS_2 crystals on the surface. By interrupting annealing to find what temperature crystals begin growing at it was found that they begin growing around 400 ^{o}C. These crystals show uniform spacings and grow as hexagon halves over the entire sample surface as shown in Fig 4.1. The XRD scans shown in Fig 4.2 hardly show any evidence of secondary phases. Distinguishing secondary phases of ZnS and Cu_2SnS_3 is nearly impossible due to peak overlap with CZTS. Due to the configuration, the diffraction signal is produced primarily by the thickness of the film and the crystals on the surface only weakly interact with the X-ray beam. In the as-deposited sample, only two peaks are strongly shown: Mo at 40.4^{o} and a 24.4^{o} peak, which is shared among ZnS, Cu_2SnS_3, and CZTS. The broadness of this peak indicates the nano-scale crystalite size formed from sputtering. The crystallite diffracting domain (*D*) for the annealed films were calculated with the Sherrer formula below and is summarized in Table 4.1 for all annealed samples also.

$$D = \frac{0.9\lambda}{\beta \cos\theta} \tag{4.1}$$

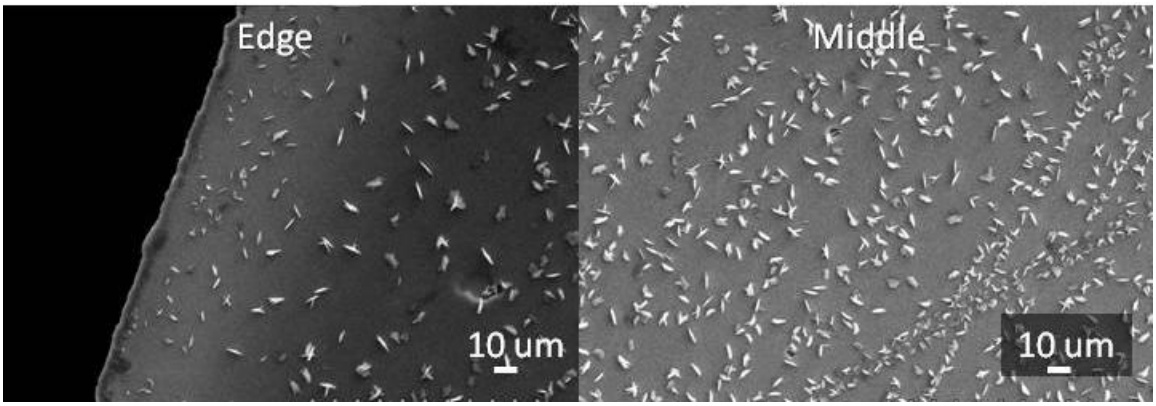

Figure 4.1: Interruption of an annealing after reaching 400 ^{o}C for 5 minutes revealed that this temperature was required before surface crystals begin forming on the surface.

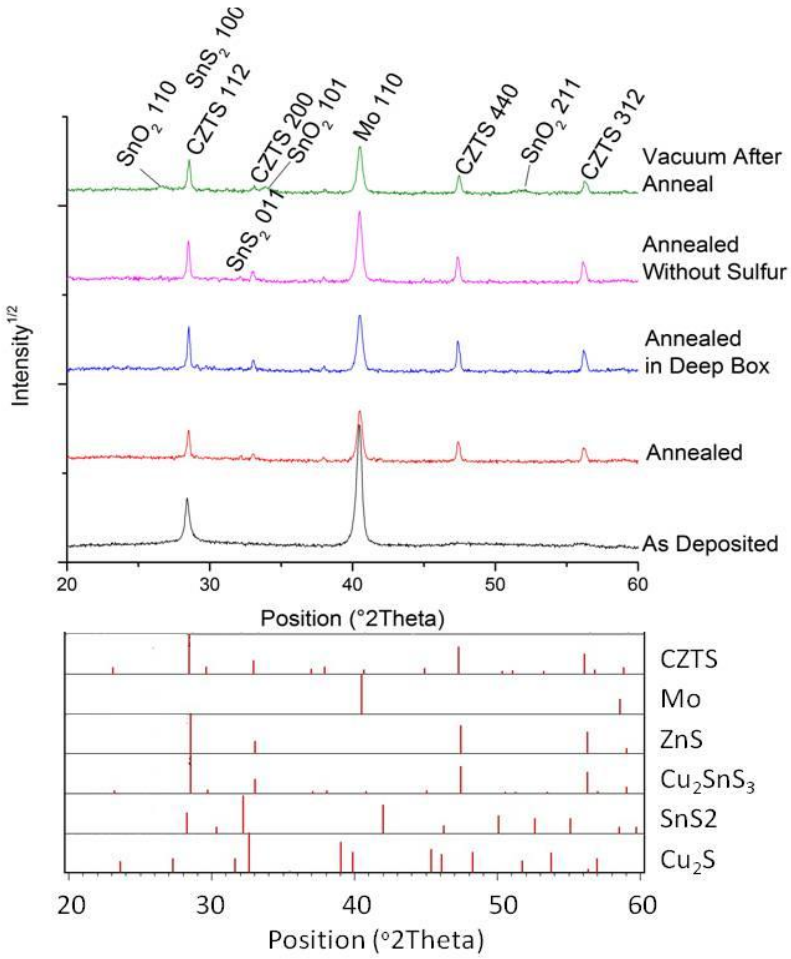

Figure 4.2: X-ray diffraction spectra of as deposited and annealed samples (upper). Overlap of X-ray peaks in standard samples makes assigning peaks difficult (lower). Film peaks are labeled as CZTS because of Raman spectroscopy results.

Table 4.1: Sherrer calculation of crystallite size produced by various annealing techniques.

Peak (^{o}2Theta)	*28.5*	*33*	*47.4*	*56.2*	***Average***	*Mo 40*
As Deposited	270		104	59	**144**	345
Annealed	602	358	1647	546	**788**	372
Annealed in Deep Box	666	798	535	795	**698**	373
Annealed without S or Sn	757	556	965	611	**722**	352
Vacuum after anneal	566	524	778	438	**577**	353

where λ is the wavelength of radiation used (CuKα 0.15418 nm) and β is the corrected (Gaussian) full width at half maximum in radian 2θ at angle 2θ. It can be seen that annealing the precursor film causes additional peaks to emerge due to grain growth which sharpens the peaks and further reacts the precursor film to form CZTS.

The ratio of the peak intensities observed do not match the standard randomly oriented powder scan and the corresponding texturing coefficients *P*, were calculated using the Harris equation [27] below for four of the main peaks observed of CZTS and are shown in Table 4.2.

$$P = \frac{I(hkl)}{\sum I(hkl)} \frac{\sum I'(hkl)}{I'(hkl)} \tag{4.2}$$

where *I(hkl)* is the integrated intensity measured and the summation is over the reflections in consideration. *I'(hkl)* represents the randomly oriented reference scan. Values for *P* are greater than 1 for reflections that are preferred and less than 1 for diminished reflections. Annealing the film shows the reduction of the initial (112) texture and the increasing randomization developing the (200) and (440) planes. Evacuating the chamber after annealing caused very broad peaks of tin dioxide to form as a result of removing the sulfur from the system and may be evidence of a leak in the chamber where

Table 4.2: Calculated values of the texture coefficient for the observed peaks of CZTS.

Plane (hkl)	*112*	*200*	*440*	*312*
As Deposited	2.61	-	0.31	1.08
Annealed	0.69	1.12	0.95	1.24
Annealed in Deep Box	0.76	0.85	1.38	1.00
Without S or Sn	0.68	0.98	0.96	1.38
Vacuum After Anneal	0.91	0.72	0.99	1.39

oxygen can enter when placed under vacuum.

The platelets that formed on the film are of high aspect ratio with breadths 5-50 μm and thicknesses less than 500 nm and compositions shown in Fig 4.3. The spot analysis EDS spectrums collected for these crystals show primarily Sn and S with traces of Cu and Zn. This was found to be due to electron penetration through the crystal to the film at the involved accelerating voltage using the Monte Carlo simulation shown in Fig 4.4. Furthermore, the layered simulation in Fig 4.5 shows that X-ray production within the CZTS layer is significant. Using the X-ray concentration mapping shown in Fig 4.6, the crystals were shown to be a Sn-S phase distinguished from the film from the lack of Cu and Zn. Micro-Raman spectroscopy was useful for characterization because it is an optical technique which is sensitive to the phases on the surface. Table 4.3 summarizes the possible Raman shifts expected. The spectrum of these crystals in Fig 4.7 confirms the analysis and identifies it to be the hexagonal crystal berndtite, SnS_2. In the sample characterized with Raman spectroscopy, only CZTS and SnS_2 peaks were detected.

4.2 A Model for SnS_2 Surface Crystal Formation

The growth of SnS_2 platelets on the surface of the film is evidence of Sn leaving the film. This instability of the Sn species during annealing of CZTS limits the temperatures and length of time films can be annealed due to Sn losses from the film.

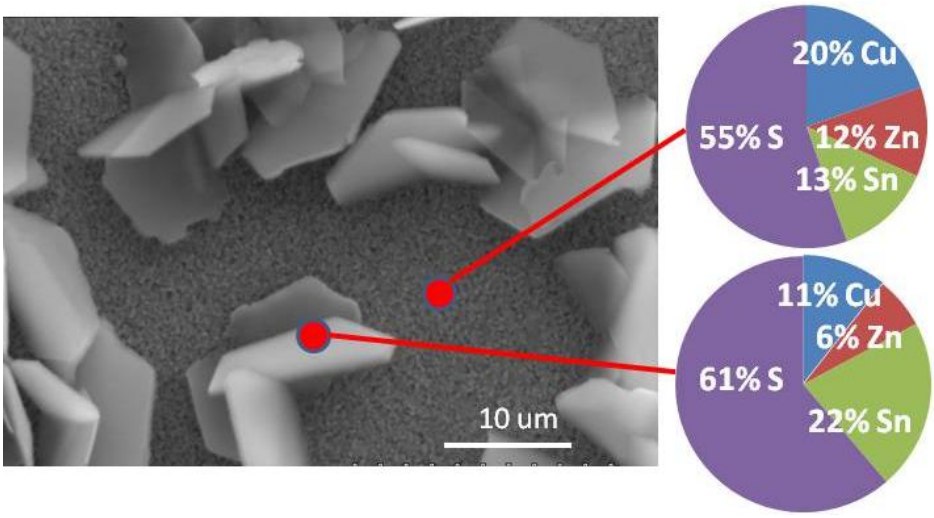

Figure 4.3: Large flat hexagonal crystals on the surface of the film with EDS compositions of the film and crystals to show approximate atomic composition at 25 kV accelerating voltage. The crystals are a primarily made of Sn and S and detection of Cu and Zn on these crystals is due to electrons penetrating through crystal.

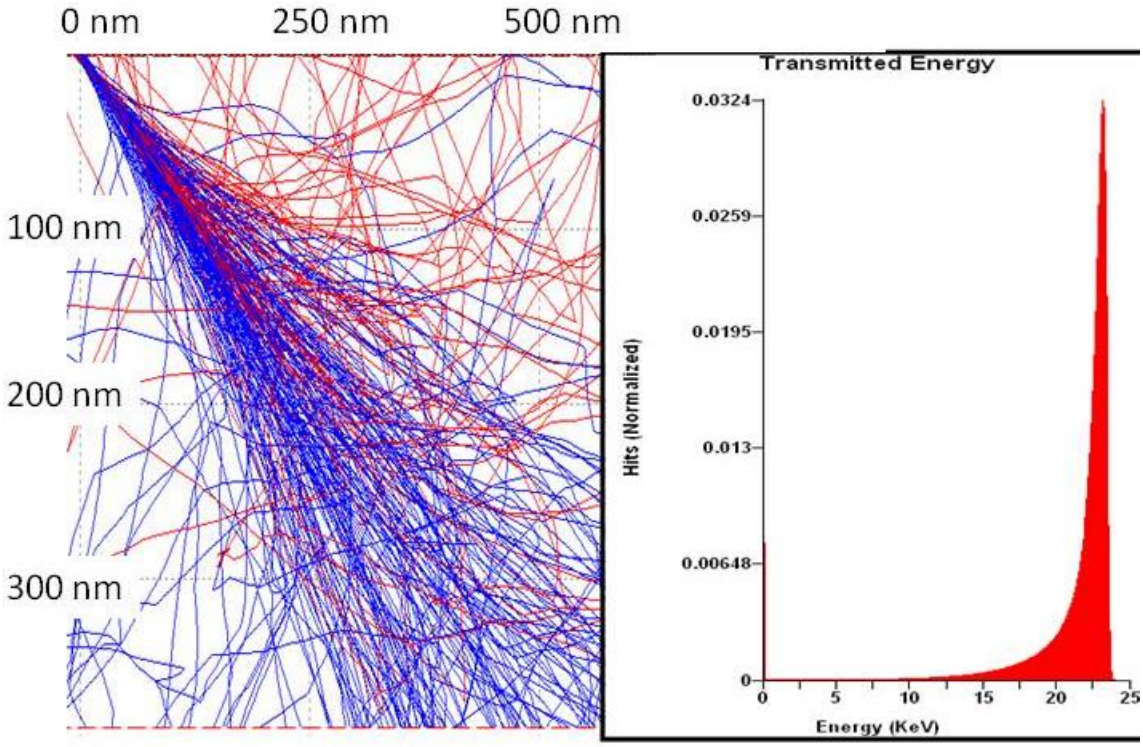

Figure 4.4: Monte Carlo simulation of e^- beam interaction with a 500 nm-thick SnS_2 platelet at an angle of 60^o. Red lines represent backscatter e^- trajectories and blue lines are absorbed or transmitted e^-s. The calculated energy distribution (inset) of the majority of transmitted e^- are greater than 22 keV; sufficient to produce X-rays in the material beneath.

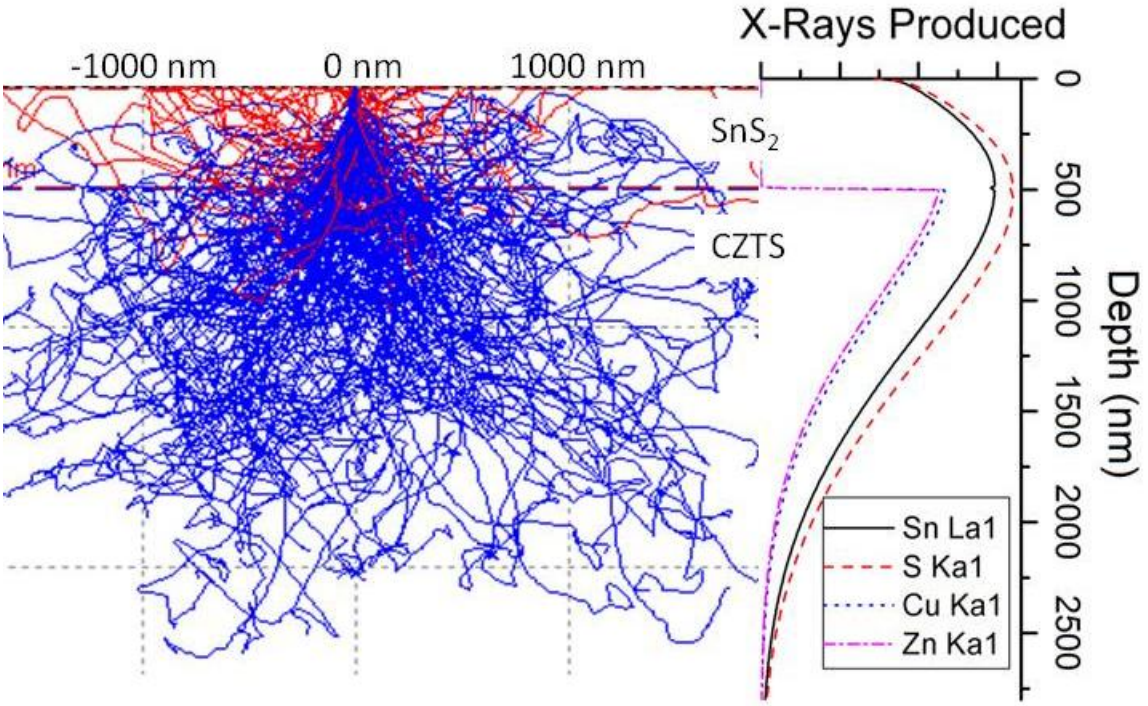

Figure 4.5: Monte Carlo simulation of e^- beam interaction with a 500 nm-thick SnS_2 layer on top of CZTS and the corresponding X-rays produced vs. depth. Penetration through the SnS_2 allows significant production of Cu Kα and Zn Kα X-rays.

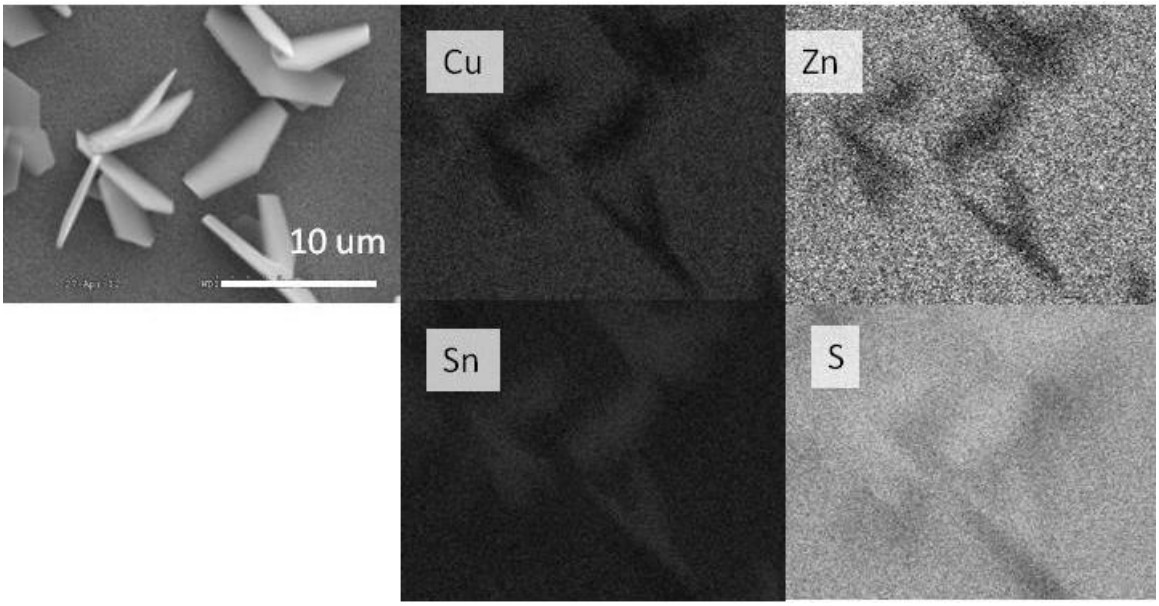

Figure 4.6 : X-ray chemical concentration map of hexagonal surface crystals identifies the crystals to be a tin sulfide compound and the film contains Cu, Zn, Sn, and S with Sn in lower concentration than the crystals.

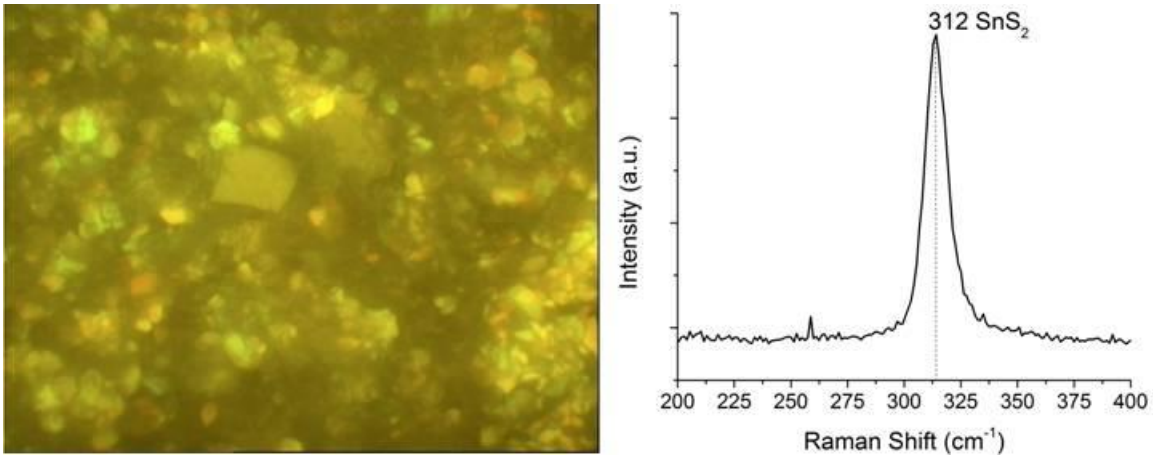

Figure 4.7: Micro-Raman spectra of an area completely covered with tin-sulfide surface crystals showing only the SnS_2 peak.

Table 4.3 Summary of Raman peak shifts.

Phase	***Raman Shift***	***References***
CZTS	289, 339, 350, 370	[28]
Cu_2SnS_3-Tetragonal	297, 337, 352	[28]
Cu_2SnS_3-Orthorhombic	318	[28]
Cu_2Sn_S3-Cubic	267, 303, 356	[28]
ZnS-Cubic	275, 352	[28]
SnS-Orthorhombic	160, 190, 219	[29]
Sn_2S_3	32, 60, 307	[29]
SnS_2-Hexagonal	215, 312	[29]
$Cu_{2-x}S$-Hexagonal	475	[28]

This section analyzes the sources of Sn and presents a model to explain why SnS_2 forms on the surface of the CZTS film and grows into platelets of high aspect ratio.

The Sn that forms into SnS_2 crystals on the surface of the film has two possible sources: the film or the reservoirs in the boat. Assuming the Cu and Zn content in the film to be constant before and after annealing and the film to be homogeneous throughout the 2 μm thickness, the change in the concentration of Sn can be estimated from the EDS results of the film in Fig 4.8 and is summarized in Table 4.4 along with estimation of Sn contained in the crystals calculated from crystal dimensions. Table 4.4 shows that more Sn was lost from the film than was formed on the surface therefore there is sufficient Sn from the film to form the SnS_2 crystals on the surface. This also shows that species present in the reservoirs had an effect on how much Sn was lost in the film and how much SnS_2 crystals formed.

The net loss of Sn from the film and its surface is evidence of loss by way of the vapor phase. The only Sn species with a sufficient vapor pressure in this material system is SnS. The decomposition of CZTS to produce SnS has been shown to have the highest decomposition rate via the following two step reaction [19]:

$$2Cu_2ZnSnS_{4(s)} \leftrightarrow 2Cu_2S_{(s)} + 2ZnS_{(s)} + 2SnS_{(s)} + S_{2(g)} \qquad \text{Reaction 3}$$

$$SnS_{(s)} \leftrightarrow SnS_{(g)} \qquad \text{Reaction 4}$$

Similarly, SnS_2 can also decompose through the reduction reaction

$$2SnS_{2(s)} \leftrightarrow 2SnS_{(s)} + S_{2(g)} \qquad \text{Reaction 5}$$

followed by reaction 4, or the products can be lost directly into the vapor phase

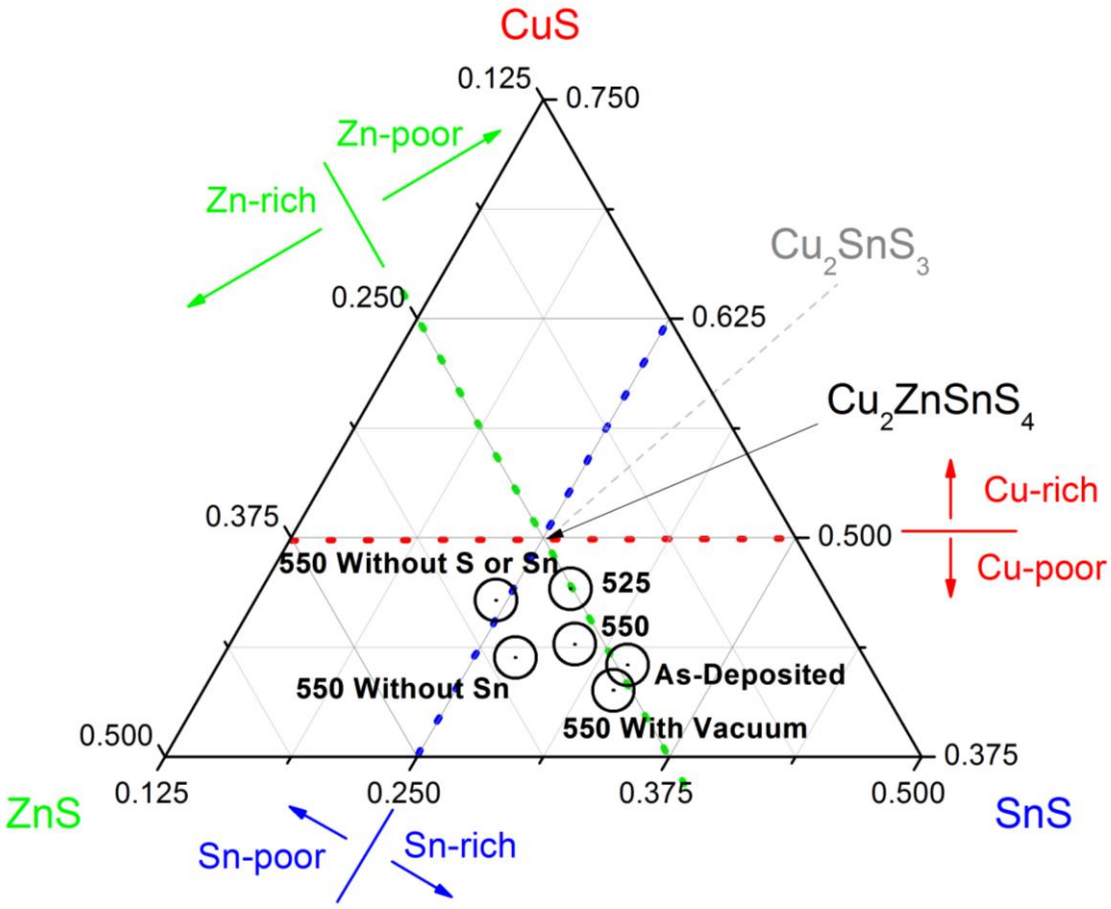

Figure 4.8: Ternary plot of film composition shifts before and after annealing procedures. Leaving out S caused Sn to be lost from film. Circles represent 5% error limits from the EDS measurement.

Table 4.4: Sn lost from film vs. Sn formed into crystals

Species added to Reservoir	Sn Lost (g/cm^3 film)	+/- geometry error	Sn Formed into Crystals (g/cm^3 film)	+/- geometry error	Average Length of Crystals (μm)
S + Sn	0.19	0.02	0.14	0.02	5.44
S	0.32	0.03	0.09	0.01	4.34
-	0.23	0.02	0.15	0.02	3.81

$$2SnS_{2(s)} \leftrightarrow 2SnS_{(g)} + S_{2(g)}$$ Reaction 6

The purpose of adding elements to the reservoirs is to the saturate the atmosphere in the boat with S_2 and SnS to reduce these decomposition reactions. In these discussions the only S species mentioned is S_2, which is the most abundant species at the annealing temperatures among the other oligomers present [30]. The reactions mentioned above are an equilibrium with the formation and decomposition as long as the species in the gas phase are present; however, the decomposition is rendered irreversible upon the removal of SnS from the system [19]. The benefit to Sn-rich growth of films is the large supply of tin-sulfide (Sn-S) species to drive CZTS equilibrium toward CZTS formation assuming sufficient S_2 to react. A sample annealed without S or Sn added in the boat would follow the decomposition reactions and show S and Sn poor composition as evidence. Fig 4.9 shows that under these conditions the sample is overwhelmed with SnS_2 crystals and the film has lost some Sn from its composition. While coverage of SnS_2 crystals increased, the average size of each of these platelets decreased. This observation compared to samples annealed with S and Sn, led to the observation that reducing the S_2 pressure increases the sticking coefficient of the Sn-S species to the film. One hypothesis is that the presence of a high concentration of sulfur during annealing saturates surface sites with adsorbed S species and hinders the sticking of SnS; whereas, annealing without sulfur would open up many locations where a Sn-S species can stick, nucleate, and grow SnS_2 crystals.

To further explore this, annealing with S and no Sn tested the extreme in reducing the sticking of SnS and while maintaining as much CZTS as possible due to the equilibrium of Reaction 3. In certain regions of the film this caused extremely thin SnS_2

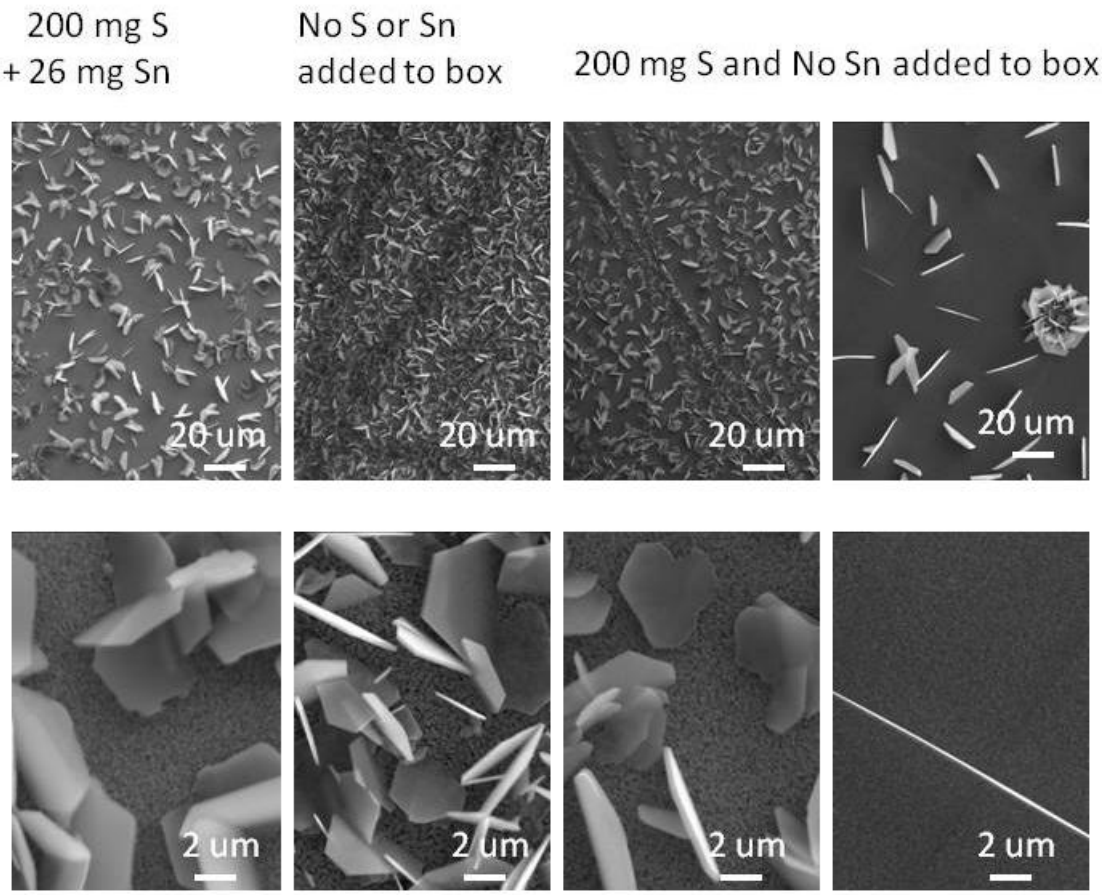

Figure 4.9: Micrographs of samples annealed with and without supplemental sulfur or tin added to the boats. Reducing sulfur increases sticking of Sn-S to surfaces causing smaller crystals and more nucleation on the film. One particular region of the sample annealed only with supplemental S showed extremely large and spread apart SnS_2 crystal (right).

crystals sparsely populating the surface as seen in the micrographs on the far right of Fig 4.9 compared to the previous samples. Growth of SnS_2 was limited primarily to the edges of the few nucleated SnS_2 crystals and debris on the sample. The SnS_2 that crystallized in this experiment could be supplied only from the decomposition reactions in the film and confirms that the primary source for the SnS_2 crystals is the film.

The shape of crystal formation provides insight on the surface free energies associated with crystallographic planes of the SnS_2 crystals and reaction kinetics. The planar growth of these crystals shows a preference for the incorporation of SnS from the

vapor to the edges rather than the large flat faces of the crystals. This can be explained by examining the crystal structure and dangling bonds associated with the crystal faces. As was confirmed by Raman, these crystals are hexagonal SnS_2 structure modeled in Fig 4.10. This crystal forms a layered structure with van der Waals forces holding the sheets together between the S anions. The interface between the basal plane sulfurs and the vapor contains no dangling bonds and is therefore a lower energy surface as compared to the prism planes. On this surface adsorbed molecules have low adhesion bonding and can readily desorb. As shown in Fig 4.11(c), S on the edges of a sheet (marked in red) are the only atoms in the crystal with unsatisfied bonds and make up the prism planes of the crystal; whereas the rest of the S and Sn have a full electron octet and are in their low energy state . The equilibrium crystal shape would maximize the low energy facets and minimizes the area of facets with dangling bonds. Concerning the growth kinetics, the dangling bonds would adsorb molecules to a much higher degree than the surface of the basal planes. In the presence of the S_2 concentrated atmosphere of the box, these high surface energy planes are saturated with S forming favorable sites for impinging SnS molecules (from the gas phase or surface diffusion from the film) to stick. At these sites the Sn oxidizes to the 4+ valence and incorporates into the crystal solid along with the S. This accounts for the high aspect ratio of these platelets seen in the micrographs.

4.3 Edge Effects

The edge effects observed on the Sn-rich films provide insight on the evolution of the surface structures on the film and potential importance of SnS_2 phases. It can be visually observed that the millimeters near the edge of annealed CZTS absorber layers are different from the majority of film, as seen on the samples shown in Fig 3.1. Under

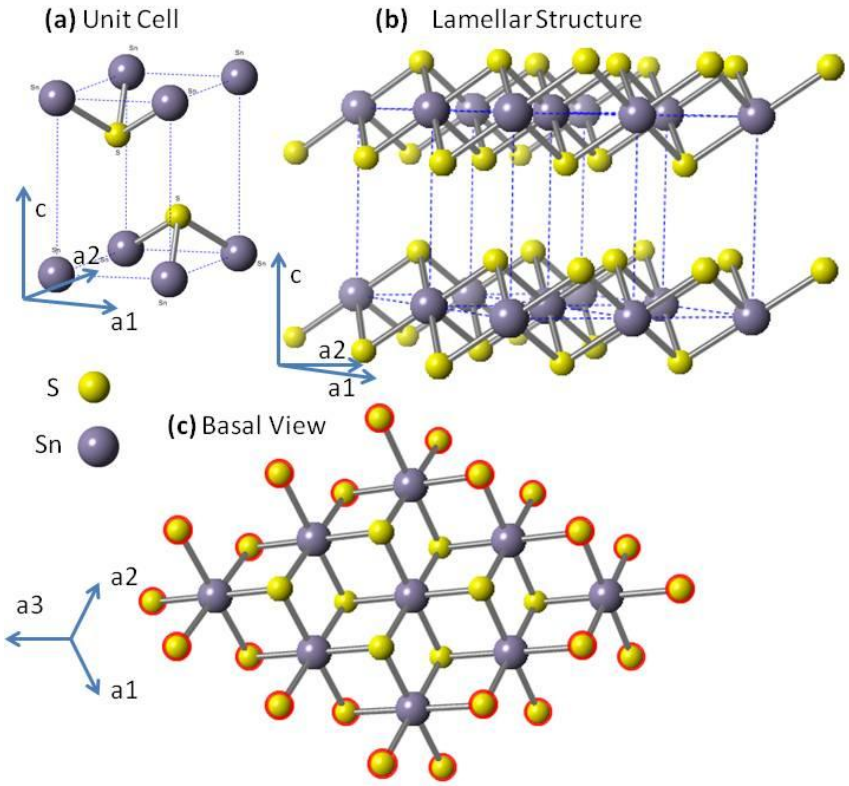

Figure 4.10: Ball and stick models of the hexagonal crystal structure of SnS_2. The unit cell (a) forms a lamellar structure (b) with van der Waals forces between sheets. Looking down the c-axis at a single sheet fully saturated with sulfur (c) shows that only the sulfurs on the edge (outlined in red) have dangling bonds and make up the growing prism planes. Crystal was simulated using CrystalMaker®[31].

SEM several different morphologies of surface phases are observed as a function of proximity to the edge. Fig 4.11 shows this progression of the surface as the edge is approached, starting with large hexagonal crystals in the bulk of the film (4.11a), then these crystals melting and coalescing together (4.11b), regions with tetragonal crystals left behind from the melt (4.11c), and regions near the edge with no surface phases and blisters formed on film (4.11d). Regions 4.11b-d show enhanced grain growth of the underlying film over the bulk region of the film (4.11a) as well as SnS_2 platelet removal. These liquid phases are produced from the SnS_2 crystals and are not from the film as found at the transition locations between these locations (not shown). Micro-Raman

spectras for these surface phases are summarized in Fig 4.12 and all show CZTS. As surface crystals change into liquid-like shapes (4.12b) we see that the SnS_2 signal nearly ceases to exist. This liquid-like phase shows no unique Raman signal and is likely due to an amorphous crystal structure producing a low signal. Similarly, the tetragonal crystal shapes have no unique signature from the CZTS background yet a clear crystal shape and therefore may be CZTS.

One potential cause of these surface crystals is explained by the thermodynamic data presented in Fig 2.4 because the Mo back contact presents a problematic reduction reaction of SnS_2 and Sn_2S_3 by forming the more stable MoS_2. Mo serves as a sink for S from SnS_2 and Sn_2S_3 at the interface. The resulting SnS cannot react to form CZTS without additional S and is consequently left to be in equilibrium with its vapor and disperse away through any available paths. This may be a cause of delamination of CZTS because adhesion at that interface could be weakened by voids left from the SnS. SnS diffusion can either collect in the film or leave through the film thickness or edges. Upon leaving the film and interacting with the highly concentrated S_2 atmosphere during annealing , the SnS can fully oxidize and form the various surface phases observed. The crystal faces discussion earlier also plays a role because only on the surface of the film is sufficient space for the preferred formation of the crystals in their equilibrium shape minimizing the surface area of the prism planes.

Possible explanations for the amorphous melted phases can be seen from the Sn-S phase diagram shown in Fig 4.13, when at elevated temperatures, the SnS_2 could decompose into a liquid melt with the loss of S. Upon cooling, the droplet solidifies into the two phase region of SnS and Sn_2S_3. In many of these liquid-like surface features

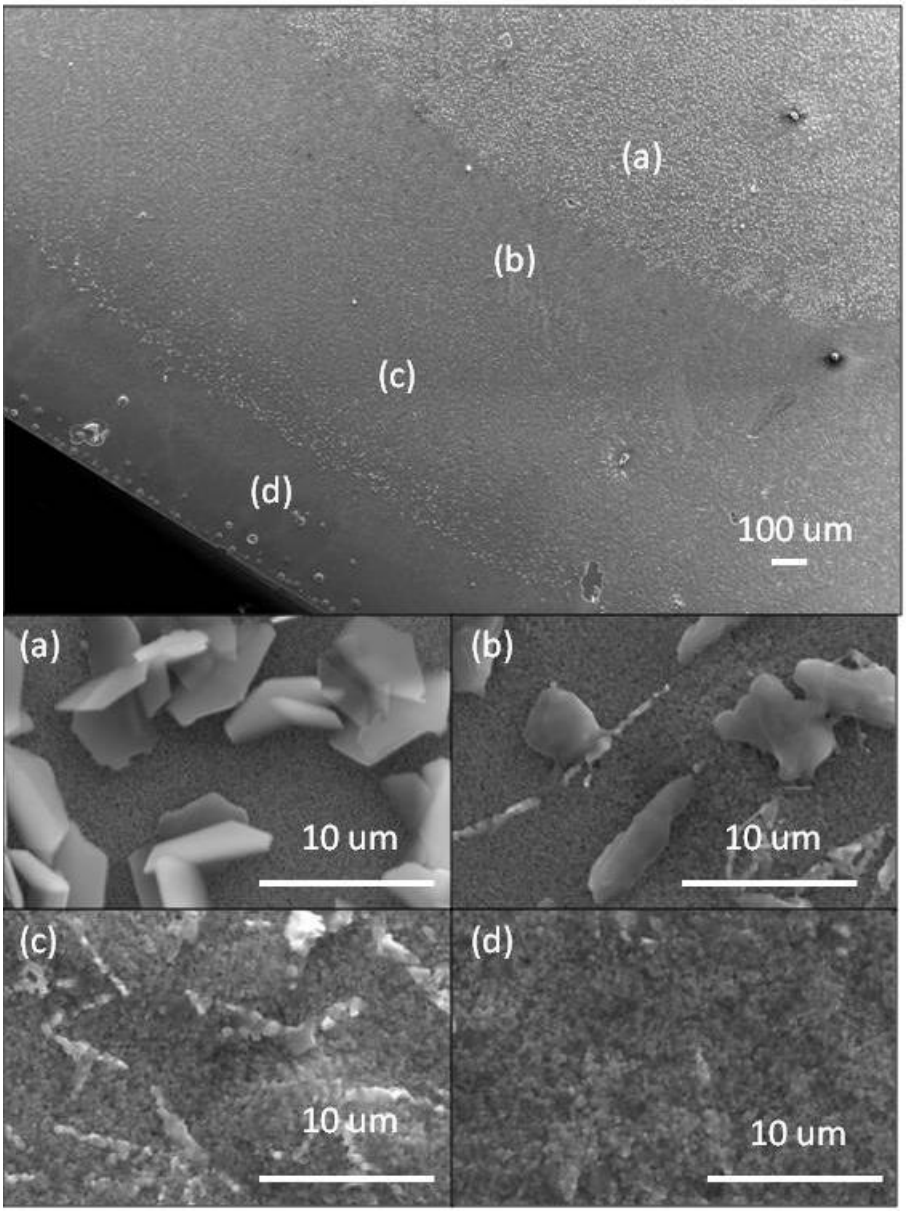

Figure 4.11: Areas of samples near edges show edge effects of morphological changes of SnS_2 crystals and enhanced grain growth of absorber. The morphology progresses from (a) large hexagonal crystals covering almost the entire film with a small grained microstructure <100 nm to (b) a region with defined grains <300 nm in size and large droplets formed on the surface from melted crystals to (c) a region marked with scars from surface phases and enhanced microstructure with grain sizes <300 nm to (d) a crystal free region with a film with grain <100nm.

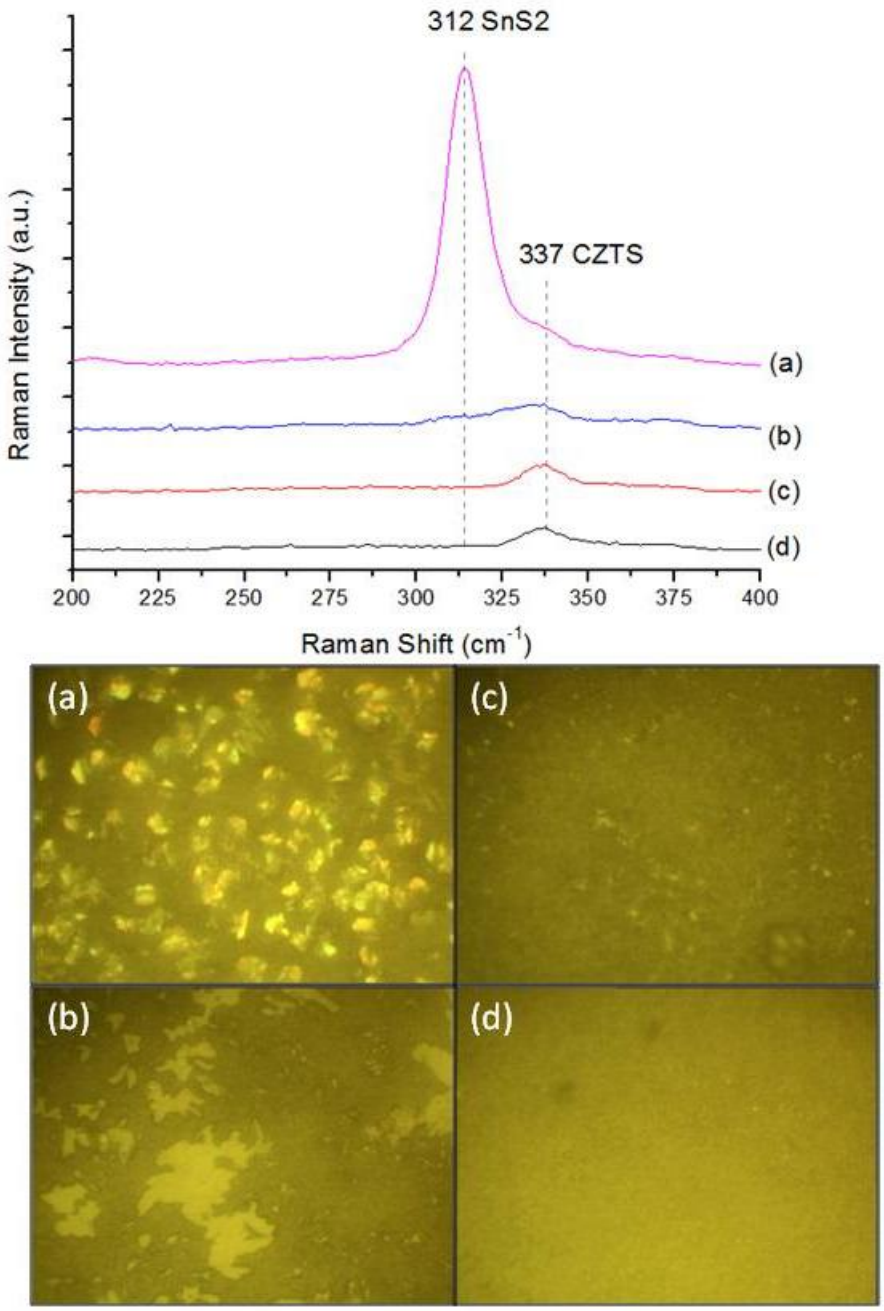

Figure 4.12: Micro-Raman spectra of different surface morphologies encountered while approaching the edge of a sample. The center of the film shows (a) large SnS_2 crystals which provide a strong signal. The signal measured from (b) coalesced liquid-like morphologies is dominated by the CZTS film beneath and shows that SnS_2 is changing into either an amorphous phase or phase with low Raman signal. The film with (c) blocky remnants left from liquid-like phases and (d) film near edge with no surface phases both only show a CZTS Raman peak.

needles can be seen as in Fig 4.14. Although these are too small to pinpoint with micro-Raman or EDS, based on the phase diagram and the observations from [29], the liquid-like phases look like SnS with Sn_2S_3 needles embedded inside caused by composition in the L_2 region of Fig 4.13 cooling into the two phase region. Samples etched in KCN solution show loss of some of these needles (4.14c and d). From the element concentration map in Fig 4.15, the crystals left on the surface show no difference in composition from the underlying film agreeing with the Raman data, but may be skewed from the high penetration depth of the e^- beam.

The grain size of many of these block-like crystals is larger than the film beneath them. The EDS and Raman analysis showed no compositional difference from the CZTS film beneath. The cause of their formation can be seen in Fig 4.16 at the interface between the SnS_2 surface crystals and the CZTS film. At this interface, Cu and Zn species diffuse from the CZTS into the SnS_2 crystal and form CZTS. This is only observed near the edges of the film where temperatures are higher. Fig 4.16 also shows that after removal of the platelet through melting, the CZTS remnant is left. This shows some optimum annealing procedures for CZTS film formation, because only where there are higher temperatures, the thermally activated diffusion of species is enough to create this unique large grained formation. However, because the CZTS formation is not observed from interfaces with the melted features, this phase does not participate in forming CZTS, so temperatures should be kept low enough to avoid the of melting the SnS_2.

A thermal gradient was applied to the film using the aluminum foil mask. This affected the distance from the edge that these different morphologies took place as well

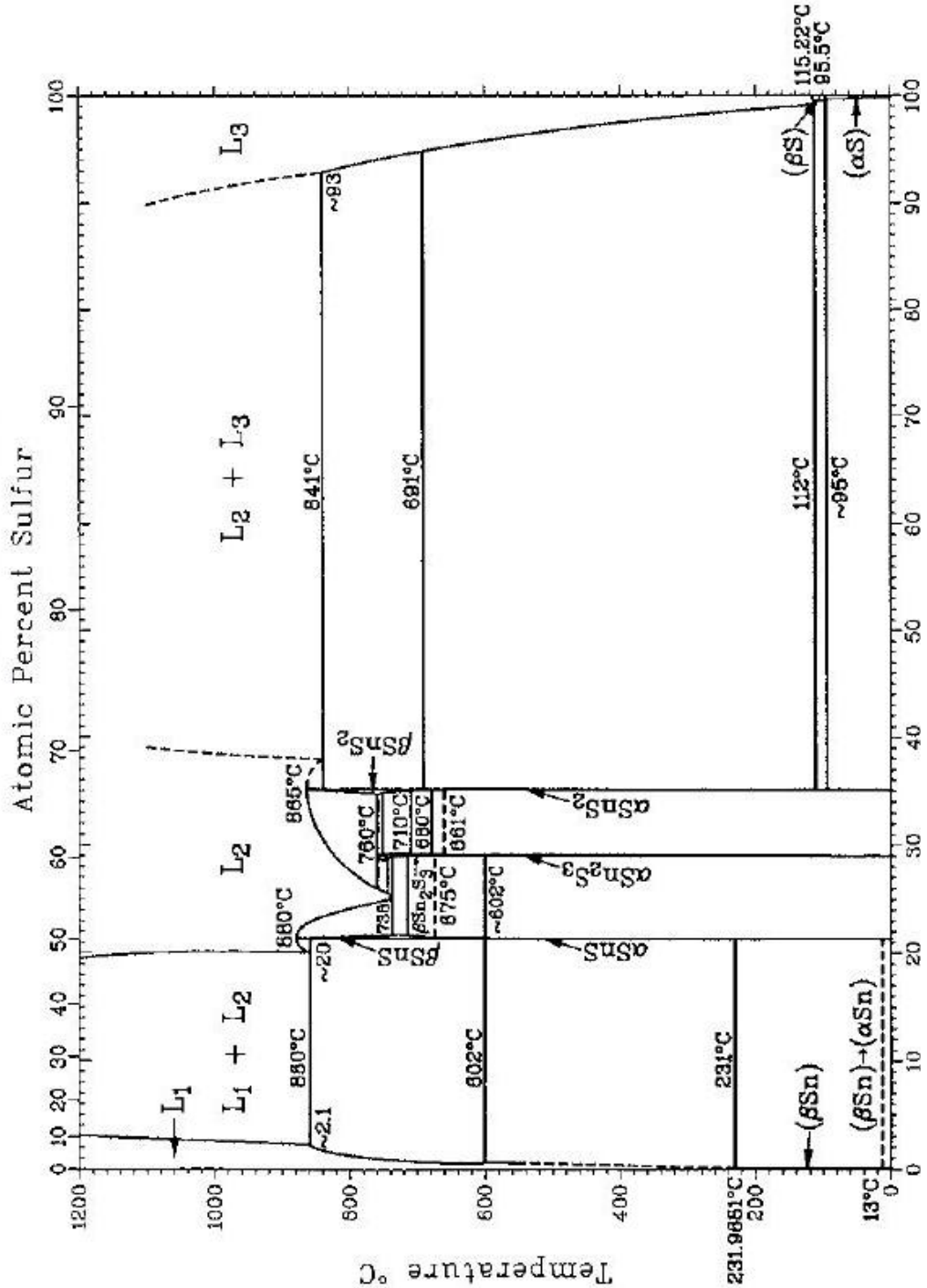

Figure 4.13: Sn-S phase diagram. Elevated temperatures and loss of S at the edges can move the equilibrium SnS_2 phase into the L_2 region, or large additions of S can lead to a solution in the L_3 region. From [32], used with permission.

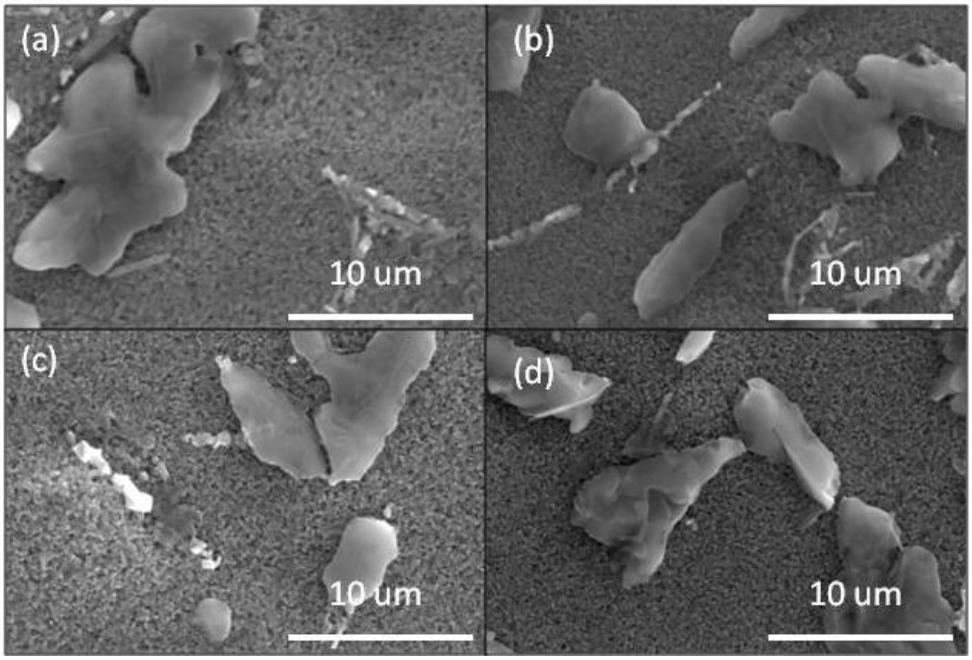

Figure 4.14: Micrographs of liquid-like surface phases before (a and b) etching and after (c and d) etching. Etching this sample in KCN for 5 minutes showed some removal of the needles from the droplets. Melting of hexagonal SnS_2 platelet structures leave blocky crystals as they move and coalesce at high temperatures.

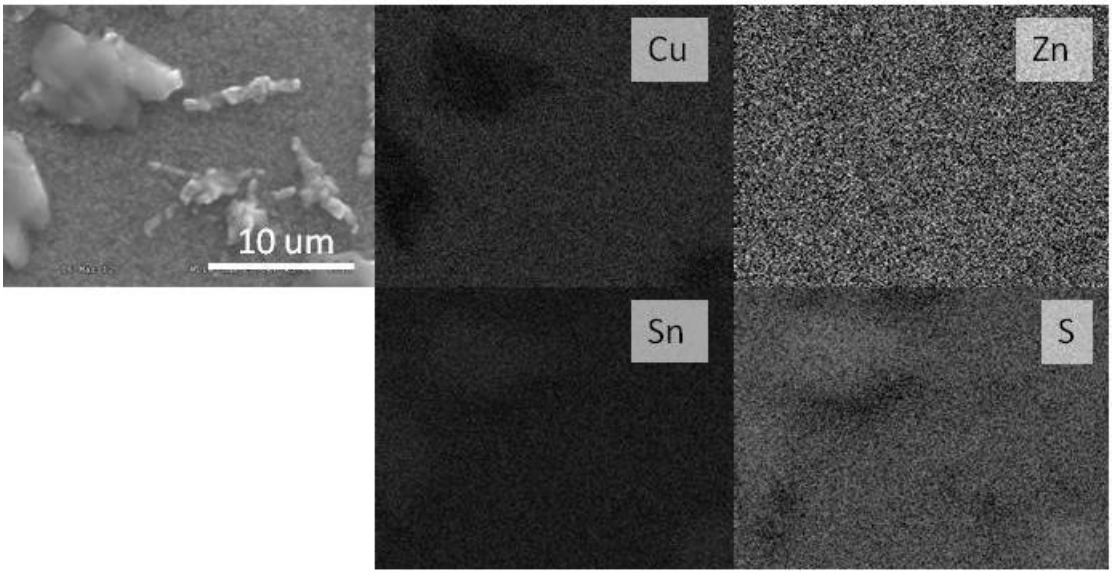

Figure 4.15: EDS elemental map of liquid-like formations and the blocky crystals left behind from their movement and coalescence. The liquid-like formations are a Sn-S phase and the crystals left behind show no contrast with the CZTS absorber meaning either it is CZTS or so small the majority of electrons from in the SEM are interacting with the absorber beneath. The lack of Zn contrast also makes it difficult to know whether the remnant crystals are CZTS or Cu_2SnS_3.

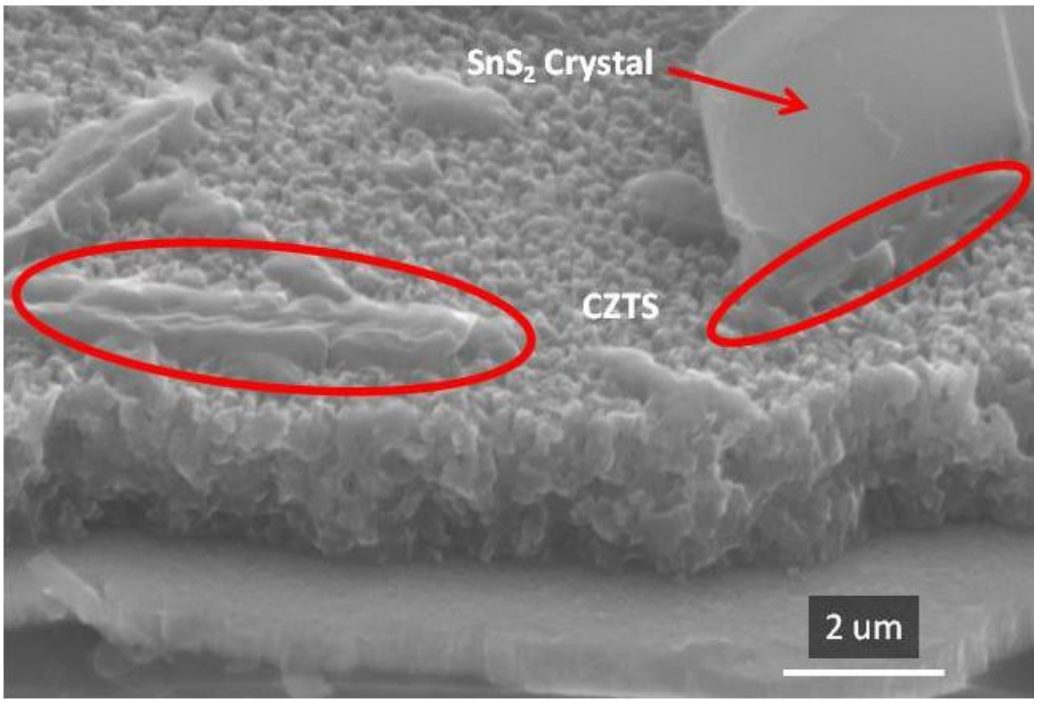

Figure 4.16: Cross-sectional micrograph showing a SnS_2 crystal in contact with the CZTS absorber on the right. The interface between the absorber and the SnS_2 fluxes a large grained structure that does not melt or remove with majority of Sn-S liquid phase near the edges. These remnants retain the shape of the interface between the SnS_2 crystals and the absorber layer, areas of these scars can be found near the edges of the entire samples usually along with droplet structures. Diffusion of Cu and Zn species from the film into the SnS_2 crystal forms this phase and is likely CZTS or Cu_2SnS_3 because of high diffusivity of Cu species at this temperature.

as the size of the surface crystals. The measurements shown in Fig 4.17 show the approximate distance from the edge in which different phases occur. Crystal morphology changed from the hexagonal crystals in the bulk, to the melted Sn-S phase, to disappearing near the edge. Lengths of these regions were longer on the hotter side of the sample, supporting the hypothesis that the edges of the film are hotter than the middle region, as well as that edge effects are contributed by a thermally activated process.

The effect this had on the morphologies is shown in Fig 4.18. The warmer side of the sample was able to grow larger crystals than the cooler side. One particular region on

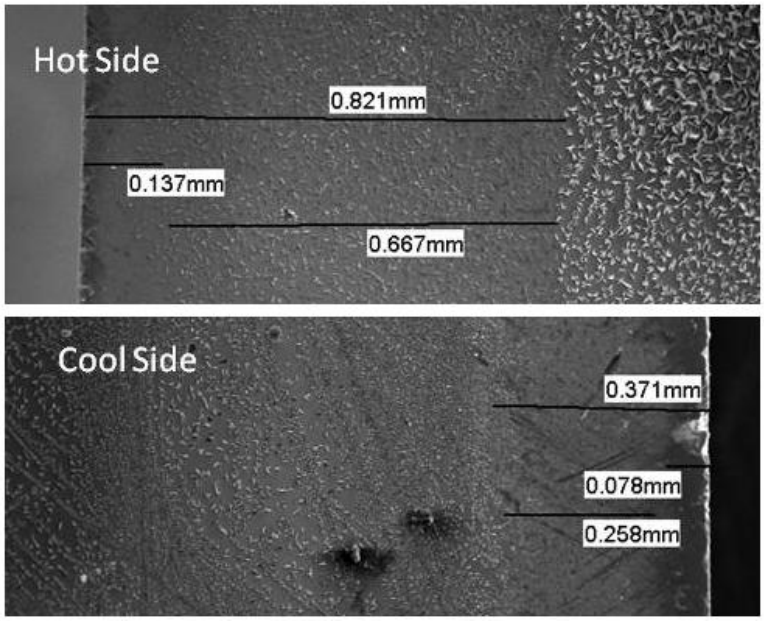

Figure 4.17: Micrographs of the edge effects dependence on temperature. The hot side of the sample shows lengths of characteristic regions to be greater than those for the cool side. SnS_2 crystals also are larger than those grown on the cool side. This shows that extraction of Sn-S and crystallization on the film is temperature activated.

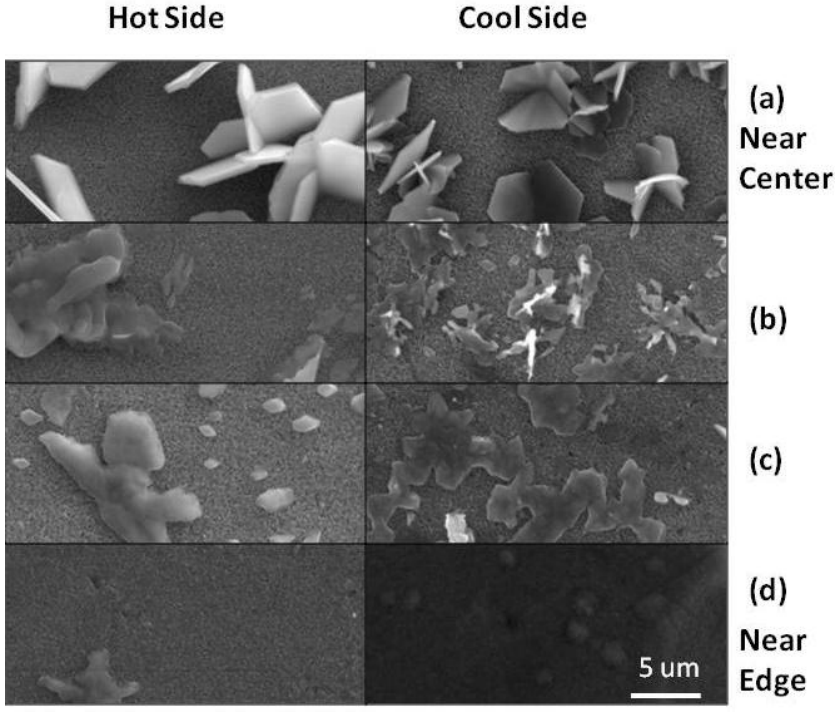

Fig 4.18: Comparison of morphology evolution between hot and cool regions of the Sn-rich film during annealing. Size of crystals is dependant temperature during annealing. Thermal decomposition rather than melting of crystals is observed in (b) on the cool side.

the cool side shown in Fig 4.18(b) has SnS_2 crystals that decomposed into a gas phase rather than forming in the liquid phase. This observation shows there in addition to forming a liquid phase, decomposition into SnS can be favored at the proper temperature and partial pressures of S_2 and SnS. Therefore thermal etching under these conditions may be used to remove SnS_2 crystals from the surface. This will require lower temperatures than annealing and effective extraction of SnS vapor from the boat in order to prevent recrystallization.

The dimensions of the box also play a role in the length of the edge effects observed. In most experiments a shallow box was used with the film nearly in contact with the lid of the box. The lid is the hottest part of the system because it is the focus of the optics of the lamp. When a deeper box with 3 mm clearance was used, edge effects were extended to those shown in Fig 4.19. These edge effects are also characterized by three distinct abrupt regions: first the bulk of the film covered with large hexagonal SnS_2 crystals; secondly closer to the edge, a region with the melted formations; and thirdly, no crystals are found near the edges. In the shallow boat, heat is conducted directly through the lid to the sample in the shallow box, whereas the deeper box has a higher thermal resistance through the air gap and is a slightly lower temperature. Because the heat source is above the samples, the system is stabilized against convection currents. It is not understood why this air gap extends the edge effects, when previously the cooler temperature reduced those lengths.

4.4 Etching of SnS_2

Fabricating a cell with SnS_2 surface crystals would cause multiple problems including covering portions of the absorber layer from incoming light, interfering with

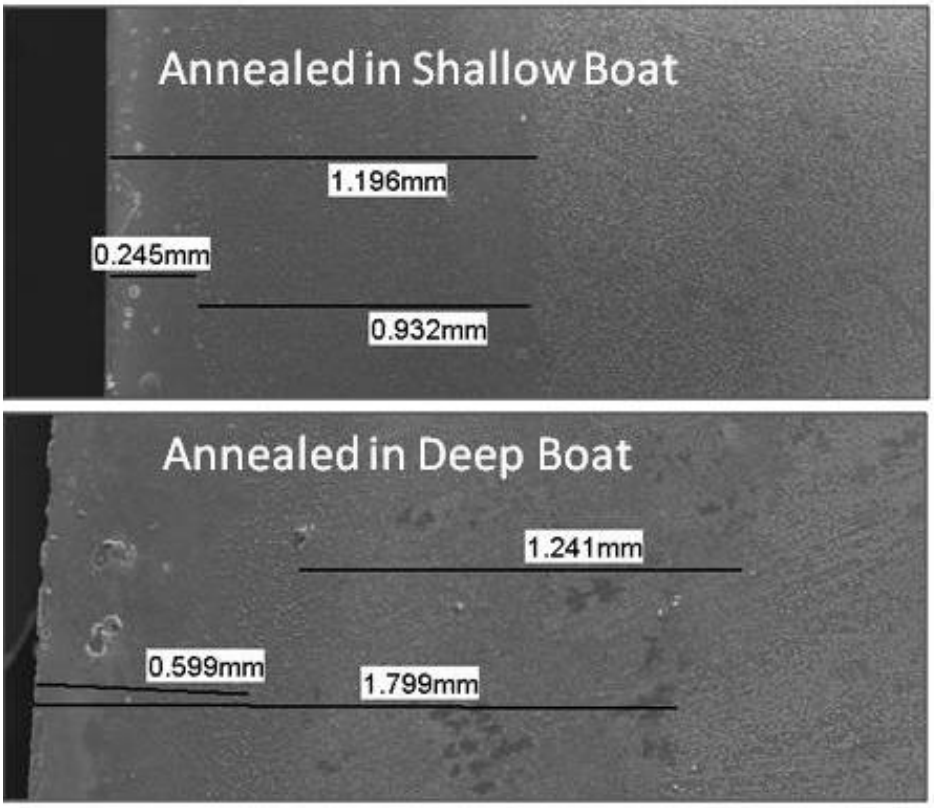

Figure 4.19: Micrographs showing the effect of using a deeper boat vs. a boat with the sample in contact with the lid. The sample in the deeper box showed longer regions without surface phases and melted phases.

further processing steps such as sputtering of ZnO, and forming deleterious junctions. Removal of these phases is essential for making these absorbers adequate for devices. Methods explored included using wet chemical etching techniques and a thermal etching technique. The thermal etching route has revealed some insight on the nature of the formation and decomposition of these crystals and the behavior of tin sulfide phases during annealing.

Wet chemical etching is routinely used for removing Cu-S secondary phases used to grow large grains. Leaving these phases in the film ruins photoconductivity measurements because of recombination of e^-/h^+ pairs at interfaces between CZTS and Cu-S [33]. In the CIGS system, a KCN aqueous solution selectively etches Cu-S phases

with 5 orders of magnitude higher etch rates than the CIGS phase itself [34]. Similarly it has been employed with CZTS and has become a fundamental step in fabrication of functioning cells. However, this etching solution of KCN does not affect the SnS_2 or Sn-S phases that grew on the surface of the film as can be seen in Fig 4.20. The effects of using an NH_4OH and HCl etching solutions are shown in Fig 4.21 for various durations. Use of a basic solution of NH_4OH also resulted in low etch rates unsuitable for removing surface phases. The acidic HCl solution on the other hand showed etching of the surface crystals and the film. Incomplete removal of the surface phases before sufficient damage was done to the film renders this solution also unsuitable for removing surface phases.

As an alternative etching technique, thermal etching was noticed in certain samples during the annealing stage (Fig 4.20b). Due to the decomposition of SnS_2 and volatile SnS phase, it is removable at elevated temperatures. Difficulty lies in isolating the decomposition of SnS_2 shown in Reaction 2 while doing minimal damage to the CZTS film by the Reaction 3. The reaction rate of Reaction 3 is dependent on the partial pressure of S_2 and has been found to be the dominant decomposition reaction [19]. Reaction 2 on the other hand depends also on SnS partial pressure; thus the reaction rates are going to be controlled by both the S and SnS species in the vapor. Etching requires the ability to remove the SnS vapor from the system inside the box while maintaining a high pressure of S in the box to prevent decomposition of CZTS. The sample shown in Fig 4.22 was produced by pulling vacuum on the annealing chamber at elevated temperatures to remove S_2 and SnS vapor to drive the decomposition in Reaction 1. This was successful in damaging the SnS_2 however a Sn phase still existed with a grainy structure in its place. Raman of this film, Fig 4.23, had no trace of the SnS_2 peak and left

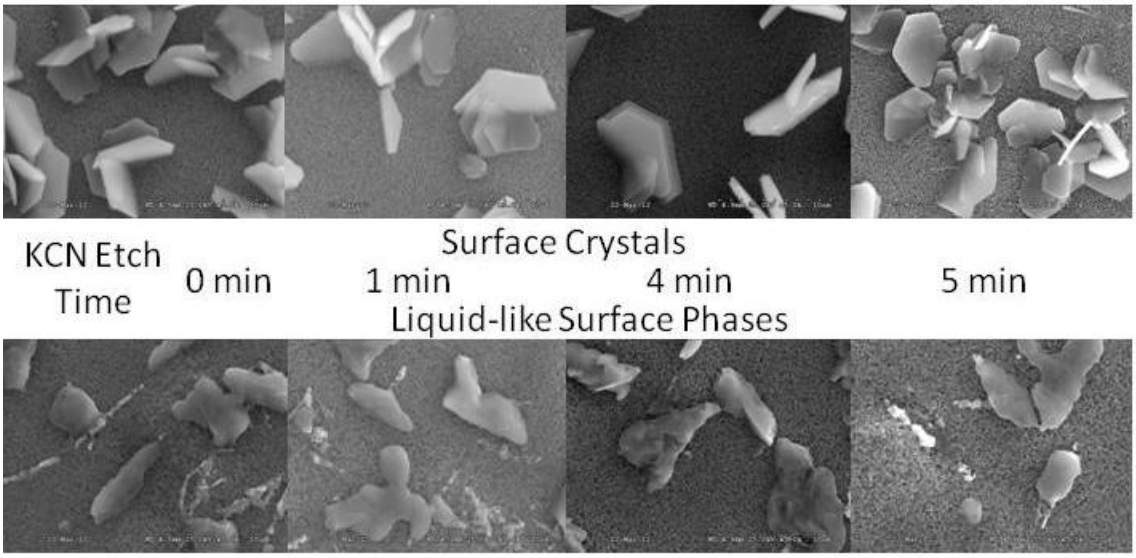

Figure 4.20: Etching of SnS_2 surface crystals (top) and liquid-like phases (bottom) in 5 wt% aqueous KCN solution shows little etching. Small amount of etching to form pits on the liquid-like phases appears.

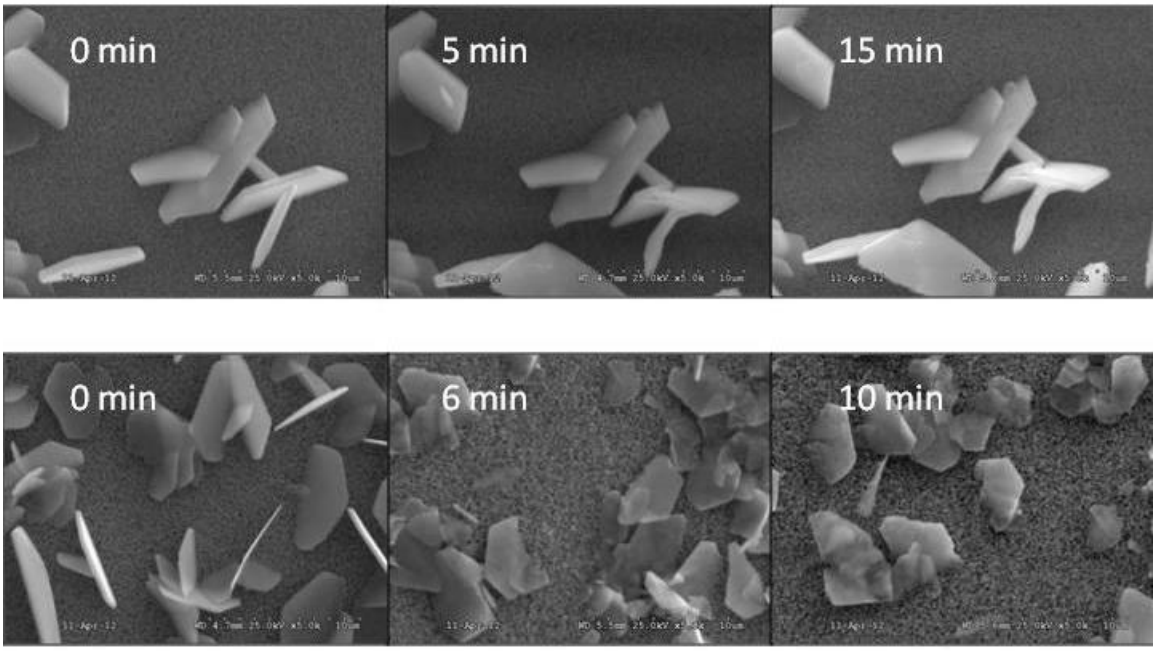

Figure 4.21: Micrographs of samples etched in basic and acidic solutions. Etching in a basic solution of NH_4OH (top) shows little etching. Etching in an acidic solution of HCl (bottom) showed rapid removal of loose platelet structures and etching of remaining platelets to form rounder shapes. Acidic solution also showed considerable damage to the film surface.

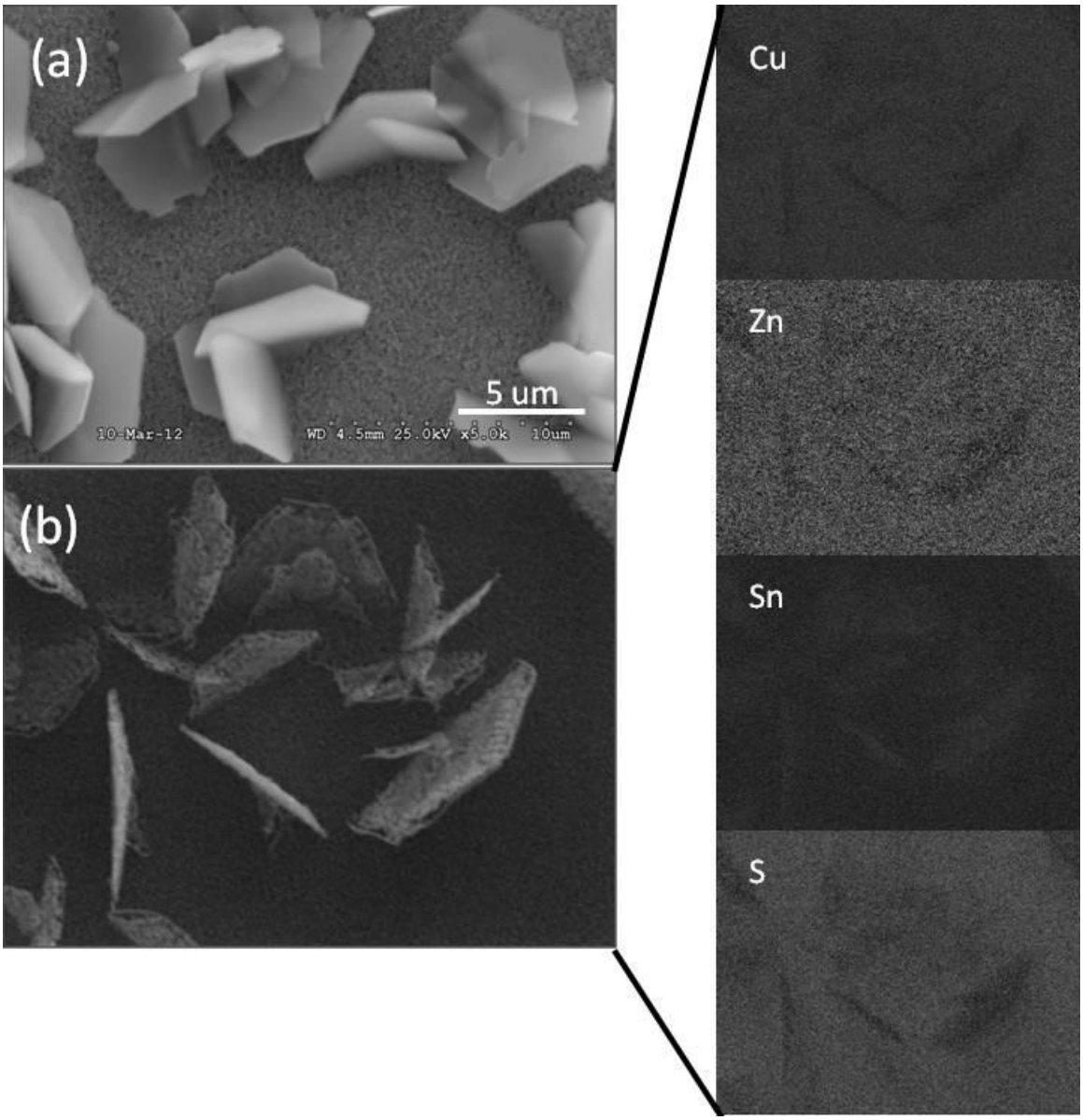

Figure 4.22: Pulling vacuum during annealing decomposes the SnS_2 phases in (a) to crumbly Sn-S phase (b) which is sulfur-poor. The compositional element mapping shows less sulfur in these crystals than even in the film.

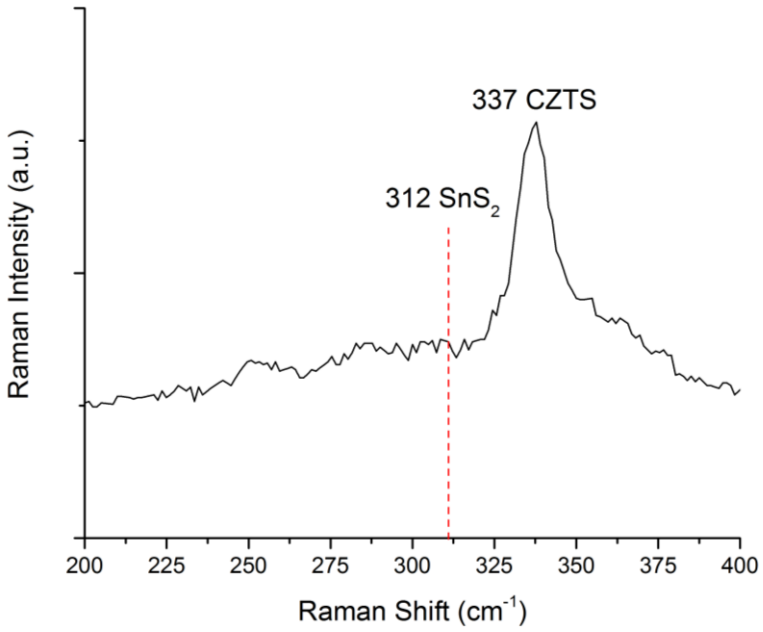

Figure 4.23: Raman spectrum of thermal etched film showing only CZTS phase and complete removal of SnS_2 phase. No other peaks are defined which prevents identification of crumbly Sn phase left where SnS_2 decomposed.

only the CZTS peak. This still leaves the grainy phase unidentified and with continued work this phase might prove to be easier to remove than the SnS_2.

CHAPTER 5

CONCLUSION

Commodity material solar cells such as CZTS are the key to widespread proliferation of solar energy by offering large scalability and reduced production costs. Sn-rich compositions provide a different approach to address the instabilities of the Sn-species during annealing of the precursor absorber layer of the cell. This work addressed a few of the difficulties associated with using Sn-rich CZTS in solar cells.

Annealing samples in various conditions revealed the role adsorbed S plays in hindering nucleation and improving incorporation of SnS onto the edges of the hexagonal crystals. Edge effects of surface phases of the film were found to be enhanced by warmer annealing temperatures. In addition, a phenomenon was discovered near the sample edge where diffusion of film species into platelets grew long continuous grains at the interface between platelets and the CZTS film.

Removal of the Sn-S surface phases was also explored by using common wet chemical etching techniques that proved inadequate for removing these phases. Thermal etching proved effective in targeting SnS_2 surface crystals and further research may prove the viability of this option.

Additional work on this topic includes testing how film strain affects the formation of edge effects because strain can be relaxed at the edges of samples. Another

aspect to investigate would involve using a controllable H_2S source for the sulfur to maintain a constant S pressure throughout the annealing as opposed to the fluctuating source used herein to see precisely how S pressure affects SnS_2 crystal formation. Lastly, the observation of diffusing species into SnS_2 to form CZTS can be studies to understand the mobility of species for application in layered precursors.

With these investigations on the Sn-rich growth of CZTS thin-film absorbers some of the key problems associated have been discussed and solutions have been attempted. Although a definitive solution to remove surface phases was not found potential routes have been suggested that require additional experimentation. With further understanding of this portion of the CZTS phase diagram Sn-rich growth may become a practical route for synthesizing earth-abundant CZTS solar cells.

REFERENCES

[1] N.S. Lewis, D.G. Nocera, Proceedings of the National Academy of Sciences of the United States of America 103 (2006) 15729-15735.

[2] S. Mehta, PV News Annual Data Collection Results: 2010 Cell, Module Production Explodes Past 20 GW, greentechsolar, 2011.

[3] L.L. Kazmerski, Journal of Electron Spectroscopy and Related Phenomena 150 (2006) 105-135.

[4] S. Olsen, NREL confirms world-record 43.5% efficiency on Solar Junction's CPV cell, 2011.

[5] V. Fthenakis, Renewable and Sustainable Energy Reviews 13 (2009) 2746-2750.

[6] P. Sinha, C.J. Kriegner, W.A. Schew, S.W. Kaczmar, M. Traister, D.J. Wilson, Energy Policy 36 (2008) 381-387.

[7] D.A.R. Barkhouse, O. Gunawan, T. Gokmen, T.K. Todorov, D.B. Mitzi, Progress in Photovoltaics: Research and Applications 20 (2012) 6-11.

[8] K. Ito, T. Nakazawa, Japanese Journal of Applied Physics, Part 1: Regular Papers and Short Notes and Review Papers 27 (1988) 2094-2097.

[9] V.S. Arunachalam, E.L. Fleischer, MRS Bulletin 33 (2008) 261.

[10] H. Chia-Hua, Journal of Physics and Chemistry of Solids 69 (2008) 330-334.

[11] R.B.V. Chalapathy, G.S. Jung, B.T. Ahn, Solar Energy Materials and Solar Cells 95 (2011) 3216-3221.

[12] Q. Guo, G.M. Ford, W. Yang, B.C. Walker, E.A. Stach, H.W. Hillhouse, R. Agrawal, Journal of the American Chemical Society 132 (2010) 17384-17386.

[13] R. Scheer, H.-W. Schock, Chalcogenide Photovoltaics, Wiley-VCH, Germany, 2011, p. 150.

[14] J. Li, D.B. Mitzi, V.B. Shenoy, ACS Nano 5 (2011) 8613-8619.

[15] T. Tanaka, A. Yoshida, D. Saiki, K. Saito, Q. Guo, M. Nishio, T. Yamaguchi, Thin Solid Films 518 (2010) S29-S33.

[16] K. Ramanathan, G. Teeter, J.C. Keane, R. Noufi, Thin Solid Films 480–481 (2005) 499-502.

[17] S.B. Zhang, S.-H. Wei, A. Zunger, H. Katayama-Yoshida, Physical Review B 57 (1998) 9642-9656.

[18] H. Katagiri, K. Jimbo, S. Yamada, T. Kamimura, W.S. Maw, T. Fukano, T. Ito, T. Motohiro, Applied Physics Express 1 (2008) 0412011-0412012.

[19] J.J. Scragg, T. Ericson, T. Kubart, M. Edoff, C. Platzer-Björkman, Chemistry of Materials 23 (2011) 4625-4633.

[20] A. Ennaoui, M. Lux-Steiner, A. Weber, D. Abou-Ras, I. Kötschau, H.W. Schock, R. Schurr, A. Hölzing, S. Jost, R. Hock, T. Voß, J. Schulze, A. Kirbs, Thin Solid Films 517 (2009) 2511-2514.

[21] T.K. Todorov, K.B. Reuter, D.B. Mitzi, Advanced Materials 22 (2010) E156-E159.

[22] R. Scheer, H.-W. Schock, Chalcogenide Photovoltaics, Wiley-VCH, Weinheim, Germany, 2011, pp. 3, 150.

[23] V.D. J., C.J. R., Mineral Chemistry of Metal Sulfides, Cambridge University Press, 1978, p. 494.

[24] G. Liu, T. Schulmeyer, J. Brötz, A. Klein, W. Jaegermann, Thin Solid Films 431–432 (2003) 477-482.

[25] J.J. Scragg, Conversion of Precursors into Compound Semiconductors

Copper Zinc Tin Sulfide Thin Films for Photovoltaics, Springer Berlin Heidelberg, 2011, pp. 59-110.

[26] D. Drouin, A.R. Couture, D. Joly, X. Tastet, V. Aimez, R. Gauvin, Scanning 29 (2007) 92-101.

[27] D. Brandon, W.D. Kaplan, Microstructural Characterization of Materials, John Wiley & Sons Ltd., Sussex, England, 2008.

[28] P.A. Fernandes, P.M.P. Salomé, A.F. da Cunha, Thin Solid Films 517 (2009) 2519-2523.

[29] L.S. Price, I.P. Parkin, A.M.E. Hardy, R.J.H. Clark, T.G. Hibbert, K.C. Molloy, Chemistry of Materials 11 (1999) 1792-1799.

[30] H. Rau, T.R.N. Kutty, J.R.F. Guedes De Carvalho, The Journal of Chemical Thermodynamics 5 (1973) 833-844.

[31] CrystalMaker Software Ltd., Oxford, England.

[32] R. Sharma, Y. Chang, Journal of Phase Equilibria 7 (1986) 269-273.

[33] J.J. Scragg, Studies of Cu2ZnSnS4 films prepared by sulfurisation of electrodeposited precursors, Chemistry, vol Doctor of Philosophy, University of Bath, Bath, UK, 2010, p. 262.

[34] M. Weber, R. Scheer, H.J. Lewerenz, H. Jungblut, U. Storkel, Journal of The Electrochemical Society 149 (2002) G77-G84.